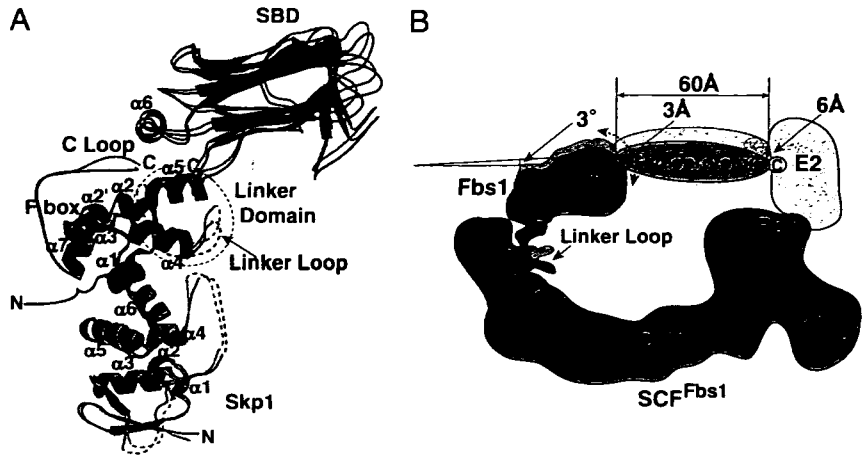

Fig. 4. Regulatory mechanism of SCF^{Fbs1} glycoprotein ubiquitination. (*A*) Comparison of the two crystal structures of the Skp1–Fbs1 complex. Skp1 (form 1), Fbs1 (form 1), Skp1 (form 2), and Fbs1 (form 2) are blue, red, yellow, and green, respectively. (*B*) Schematic representation of the model for ubiquitination on SCF^{Fbs1}. The E2 active-site cysteine and acceptor lysine residues are depicted with circled letters.

Skp2 (1.5-Å rms deviation for 27 C^{α} atoms) and β-TrCP1 (1.7-Å rms deviation for 28 C^{α} atoms), there are several differences. Helix α2 in Fbs1 is composed of two segments (α2 and α2′) separated by a turn, which causes it to bulge into the C loop of Skp1. The orientations of helices α3 and α4 of Fbs1 are similar to those of Skp2 but not to those of β-TrCP1 (Fig. 2*A*). Moreover, whereas the C-terminal region of the F-box domain of Skp2 is a loop structure, those of Fbs1 and β-TrCP1 form α-helices (α4).

The binding mode between Skp1 and the F-box domain of Fbs1 is almost identical to those between Skp1 and Skp2 (1.0-Å rms deviation for 120 C^{α} atoms) and between Skp1 and β-TrCP1 (1.1-Å rms deviation for 117 C^{α} atoms), except that the C loop of Skp1 interacts with the F-box domain through van der Waals contacts (Phe-145, Glu-149, Glu-150, Ala-151, Gln-152, and Val-153 of Skp1 interact with Val-72, Gln-73, Arg-76, Leu-77, and Leu-80 of Fbs1) (Fig. 2*B*). The positions of the Fbs1 F-box domain and α7 in Skp1 are shifted away from the N-terminal domain of Skp1 by ≈4.0 Å (Skp1–Skp2) or ≈2.5 Å (Skp1–β-TrCP1). These differences in the distances from the F-box domains to α7 of Skp1 and the C-terminal structures of Skp1 are likely due to the F-box structure.

Structure of the Glycoprotein Complex of the SBD. Ribonuclease B (RNaseB) is a glycoprotein that has a single high-mannose oligosaccharide ($Man_{6-8}GlcNAc_2$) attached at Asn-34 (19). RNaseB binds to the edge of the β-sandwich of the SBD (Fig. 3*A*). Clear electron density demonstrates the presence of $Man_3GlcNAc_2$ bound to the Fbs1 monomer, but the outer branches of the carbohydrate are disordered and not visible in the electron density map. The structure of the Fbs1-bound RNaseB, which consists of three α-helices and seven β-strands, is essentially identical to the previously reported structures of apo-RNaseB (20, 21); these structures have an average 0.59-Å rms deviation for the C^{α} positions. Similarly, the SBDs in the structures of the Skp1–Fbs1 and SBD–RNaseB complexes can be superposed with an average 0.48-Å rms deviation for the C^{α} positions, indicating that RNaseB binding does not cause any significant structural changes in the SBD.

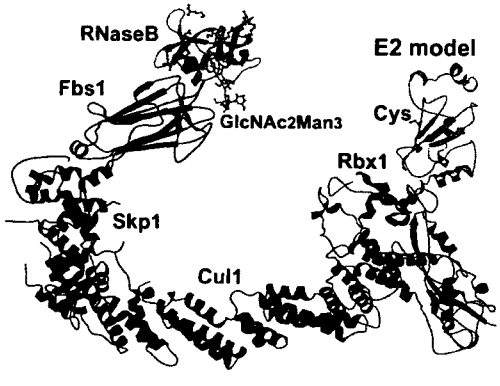

Fig. 5. Model of the SCF^{Fbs1}–RNaseB complex bound to E2. Cul1, Rbx1, Skp1, Fbs1, RNaseB, and E2 are green, orange, blue, red, cyan, and yellow, respectively. Lysine residues on the RNaseB surface are presented in ball-and-stick format and are coral.

Glycoprotein Recognition by the SBD in the SBD–RNaseB Complex. The sugar-binding surface consists of the four loops between β2 and β3, β3 and β4, β5 and β6, and β9 and β10. $Man_3GlcNAc_2$ interacts with nine Fbs1 residues (Asp-158, Asn-159, Phe-177, Arg-214, Asp-216, Tyr-279, Trp-280, Lys-281, and Phe-284) through hydrogen bonds and/or van der Waals contacts (Fig. 3 *B* and *C*). The molecular recognition mechanism between the chitobiose moiety and the amino acid residues in Fbs1 is similar to that reported previously for the SBD–chitobiose complex (17). The methyl group of the *N*-acetyl moiety from the GlcNAc (I) residue is inserted into a small hydrophobic pocket surrounded by the side chains of Phe-177, Tyr-279, and Lys-281; and the O3 atom forms a hydrogen bond with the main chain N atom of Lys-281. The GlcNAc (II) residue is stacked on the aromatic ring of Trp-280 and the O6 atom forms a hydrogen bond with the carbonyl oxygen atom of Lys-281. The two GlcNAc residues form an intramolecular hydrogen bond between the O3 atom of GlcNAc (I) and the O6 atom of GlcNAc (II). Formation of these hydrogen bonds fixes the orientation of the β(1→4)-linked GlcNAc residues. Comparison of the SBD–RNaseB complex and the previously reported SBD–chitobiose complex reveals that the substrate binding pockets (Phe-177, Tyr-279, Trp-280, and Lys-281) and the chitobiose structures can be superposed with an average rms deviation of 0.69 Å for all of the atoms (Fig. 3*D*). Only the side chain of Lys-281 has a different conformation, and it has been shown that Lys-281 is not essential for the binding to chitobiose (17). The outer mannose-binding residues of the SBD also do not exhibit significant conformational changes. We have reported that Fbs1 recognizes not only chitobiose but also the outer mannose branches (17). The O4 atom of Man(III)

Table 1. Data collection, phasing, and refinement statistics

	Skp1–Fbs1	Skp1–Fbs1/Thimerosal	Skp1–Fbs1	SBD–RNaseB
Data collection				
Space group	$P3_221$	$P3_221$	$P2_12_12_1$	$P432$
Cell parameters, Å				
a	106.7	106.6	66.2	148.6
b	106.7	106.6	111.1	148.6
c	110.2	113.7	153.3	148.6
Unique reflections	27,964	17,765	12,269	15,839
Resolution range, Å	2.40 (2.49–2.40)	2.80 (2.90–2.80)	3.50 (3.63–3.50)	2.70 (2.80–2.70)
R_{merge}	0.045 (0.327)	0.058 (0.328)	0.103 (0.225)	0.078 (0.325)
$I/\sigma I$	18.1 (2.7)	16.0 (2.2)	7.0 (4.1)	13.9 (5.2)
Completeness, %	97.7 (93.0)	95.7 (79.6)	85.2 (79.0)	99.4 (97.9)
Redundancy	5.4 (2.9)	6.2 (2.3)	2.6 (2.1)	11.8 (6.4)
Refinement				
No. of reflections	26,521		12,279	15,049
R_{work}/R_{free}	0.233/0.291		0.223/0.299	0.216/0.288
rms deviations				
Bond lengths, Å	0.010		0.022	0.026
Bond angles, °	1.33		2.08	2.51

Values in parentheses represent the highest-resolution shell.

forms a hydrogen bond with the sidechain O^{δ} atom of the Asp-216 sidechain; this hydrogen bond stabilizes the complex with the Manβ(1→4)GlcNAc$_2$ moiety. Clear electron density is observed between the β(1→4)-linked Man residue and Asp-216 in Fbs1. Furthermore, Asp-216 is conserved in other F-box proteins that contain an F-box-associated domain, suggesting that it plays a role in the recognition of oligosaccharides. Man(IV) forms hydrogen bonds with the sidechain N^{δ} atom of Asn-159 through the O2 atom and with the sidechain N^{η} atom of Arg-214 through the O5 atom. On the other hand, Man(V) protrudes from the binding site and does not interact with Fbs1. These results indicate that the GlcNAc$_2$ core, β(1→4)-linked Man(III), and α(1→3)-linked Man(IV) play significant roles in the binding to Fbs1. Whereas Man$_8$GlcNAc$_2$ is thought to be the major N-glycan among unfolded glycoproteins that are translocated into the cytosol for endoplasmic reticulum-associated degradation, our results indicate that Man$_3$GlcNAc$_2$ can be sufficiently recognized by the SCF^{Fbs1} complex. Indeed, various synthetic oligosaccharides were used to show that Man$_3$GlcNAc$_2$ and Man$_8$GlcNAc$_2$ have similar affinities for Fbs1 (22). On the other hand, the binding affinities of Man$_8$GlcNAc$_1$ and chitobiose for Fbs1 are several orders of magnitude lower than those of Man$_3$GlcNAc$_2$ and Man$_8$GlcNAc$_2$, indicating that Man$_3$GlcNAc$_2$ is required for efficient binding to Fbs1 (15, 22). Moreover, the binding site provides substrate selectivity and specificity based on its shape and hydrogen-bonding network.

There are limited contacts between the SBD and RNaseB; the interface involves only 514 Å^2 of surface-accessible area. The surface areas occupied by Man$_3$GlcNAc$_2$ and the protein portion of the substrate are 349 and 165 Å^2, respectively. In addition to the smaller contact area, the protein portion of RNaseB does not form a hydrogen bond with Fbs1, suggesting that Man$_3$GlcNAc$_2$, but not the protein in RNaseB, defines the interaction with Fbs1.

Linker Flexibility Might Accommodate a Range of Substrates. Two crystal forms were identified for Skp1–Fbs1 ($P3_221$ and $P2_12_12_1$ define form 1 and form 2, respectively). These two forms have essentially the same overall structure (rms deviation of 1.1 Å for the C^{α} atoms) (Fig. 4*A*). Whereas the Skp1 proteins are well aligned with each other, the SBD of Fbs1 in form 2 is tilted farther away from Skp1 by ≈3°. The 3° tilt angle of the SBD creates a 3-Å gap at the substrate-binding site and a 6-Å shift at the E2 active site. This flexibility seems to be due in part to the linker-domain structure of Fbs1 (Fig. 4*A*). Residues 100–103 and 113–115 are shifted significantly compared with form 1. Although the linkage between the F-box and WD40 domains does not seem to be exceedingly rigid in the yeast Cdc4 structure, deletion of helix α5 or the lengthening of helix α6 due to an insertion of amino acid residues disrupts Cdc4 function *in vivo*, suggesting that the orientation and rigidity of the linkage between the F-box and the substrate-binding domains is important for SCF function (8). In the structure of Fbs1, the interaction between α5 and the linker loop through van der Waals contacts (His-113 of the linker loop to Gln-115, Phe-119, and Arg-123 of α5) is not rigid, and residues 104–108 of the linker domain are not visible in the electron density map. This structure indicates that the linkage between the F-box domain and the SBD of Fbs1 is somewhat flexible. This feature might allow the protein to accommodate a range of substrates (Fig. 4*B*).

Discussion

In this study, we determined the crystal structures of two crystal forms of the Skp1–Fbs1 complex and the SBD–RNaseB complex at 2.4-, 3.5-, and 2.7-Å resolutions, respectively. The structure of the Skp1–Fbs1 complex illustrates a different class of F-box proteins within the SCF ubiquitin ligase model. A model of the SCF^{Fbs1}–RNaseB–E2 complex was generated simply by superposition of the Skp1 subunits from the Skp1–Fbs1 and Skp1–Cul1–Rbx1 structures (PDB ID code 1LDK), the RING-finger domains derived from Rbx1 and from the c-Cbl subunit of the c-Cbl-UbcH7 structure (PDB ID code 1FBV) (23), the E2 subunits of the c-Cbl-UbcH7 structure, and the SBD-RNaseB structure. In this SCF^{Fbs1}-RNaseB model, RNaseB points toward the E2-binding site on Rbx1 (Fig. 5). The distance between the E2 active-site cysteine and the substrate-binding site is ≈60 Å, which is similar to the value that was reported previously (7, 8, 10). Despite differences in the sizes of the substrates and the positions of ubiquitinated lysine residues, the distance between the E2 active-site cysteine and the substrate-binding site is conserved among the SCF complexes. The same mechanism that allows the E2 active-site cysteine to reach the ubiquitinated lysine residues of the substrates is used independently of the type of F-box protein.

In the case of RNaseB, the distances between the E2 active-site cysteine and the lysine residues in RNaseB are 58.6–88.4 Å in the model of the SCF^{Fbs1}–RNaseB–E2 complex, whereas the

lysine residues in RNaseB are between 5.3 and 36.9 Å away from Asn-34. RNaseB is smaller than the minimum distance required to reach E2. Actually, SCF^{Fbs1} was not able to ubiquitinate RNaseB *in vitro*. This could be because RNaseB is too small, the lysine residues are at the wrong positions, or RNaseB is fixed because of contacts between $Man_3GlcNAc_2$ and Fbs1.

One of the most important properties for ubiquitination is the rigidity of the SCF–ubiquitin–ligase complex structure, because it serves to correctly position the target protein and E2. The two crystal structures of the Skp1–Fbs1 complex described in the present study, however, show differences in the orientation of the SBD. We propose that SCF^{Fbs1} has the ability to nonspecifically ubiquitinate glycoproteins targeted to the endoplasmic reticulum-associated degradation pathway. The protein portion of a target glycoprotein bound to Fbs1 may rotate at the linkage site between the innermost GlcNAc moiety and the asparagine residue, and the acceptor lysine residue can be located at a variety of positions. In SCF^{Fbs1}, the relative motion of the linker domain between the F-box domain and the SBD might be necessary to accommodate the different positions of the acceptor lysine residues in the various endoplasmic reticulum-associated degradation substrates.

SCF^{Fbs1} is a functionally unique molecule that recognizes the innermost $Man_3GlcNAc_2$ in N-glycans as a marker of denatured proteins. Our results provide a mechanistic basis for the recognition and ubiquitination of various glycoproteins by SCF^{Fbs1}.

Materials and Methods

Protein Expression and Purification. The Skp1–Fbs1 complex was coexpressed from the pET28b plasmid (Novagen, Madison, WI) in BL21 (DE3) cells. Full-length Skp1 was expressed as a 6× His-tagged protein, and full-length Fbs1 was expressed as an untagged protein. The complex was purified stepwise by Ni affinity, anion exchange, and gel-filtration chromatography. The Skp1–Fbs1 complex was then concentrated to ≈10 mg/ml by ultrafiltration in 25 mM Tris·HCl (pH 7.5) and 1 mM DTT.

For the SBD–RNaseB complex (with SBD residues 105–297 of Fbs1), the SBD and RNaseB (Sigma, St. Louis, MO) were combined in a 1:1 molar ratio and purified by gel-filtration chromatography. Fractions containing the SBD–RNaseB complex were then concentrated to ≈10 mg/ml and used for crystallization.

Crystallization and Data Collection. Crystals of Skp1–Fbs1 and SBD–RNaseB were obtained at 20°C by using the sitting-drop vapor diffusion method. Skp1–Fbs1 crystals were grown from 2.0 M ammonium sulfate, 0.1 M sodium citrate (pH 5.7), and 30 mM chitobiose, which produced two crystal forms. The SBD–RNaseB crystals were prepared by using 2.0% (vol/vol) PEG 400, 0.1 M Hepes (pH 7.5), and 2.1 M ammonium sulfate.

Diffraction data sets for Skp1–Fbs1 and SBD–RNaseB were collected at beamline BL44XU (SPring-8, Hyogo, Japan). Data processing and reduction were carried out with the HKL program suite (24). The two crystal forms of Skp1–Fbs1 and the SBD–RNaseB crystals belong to the $P3_221$ (Skp1–Fbs1 form 1), $P2_12_12_1$ (Skp1–Fbs1 form 2), and $P432$ (SBD–RNaseB) space groups. Heavy-atom soaks of the Skp1–Fbs1 crystals (form 1) were performed in crystallization buffer with 1 mM thimerosal for 5 min. Data collection, phasing, and refinement statistics are summarized in Table 1.

Structure Determination and Refinement. The structure of Skp1–Fbs1 was determined by a combination of molecular replacement, single isomorphous replacement, and anomalous scattering with an Hg derivative. The initial single isomorphous replacement and anomalous scattering phases were calculated with SHARP (25) and then improved by density modification with DM (26). Molecular replacement with the program MOLREP (27) was used to locate the Skp1 and SBD portions of the complex with search models consisting of Skp1 from SCF (PDB ID code 1LDK) and the SBD of Fbs1 (PDB ID code 1UMH). The model was further built with the program COOT (28) and then was improved by several cycles of manual rebuilding and refinement with the program REFMAC5 (29). The structure of crystal form 2 was solved by molecular replacement using MOLREP with the refined model of form 1.

The structure of SBD–RNaseB was determined by using the molecular replacement technique, MOLREP, and the structures of the SBD and RNaseB. The refined model contains residues 123–297 of the SBD and residues 1–124 of RNaseB. Phasing and refinement statistics are summarized in Table 1. There are no residues in disallowed regions of the Ramachandran plot. Structure figures were generated by using MOLSCRIPT (30), RASTER3D (31), and CCP4MG (32).

We thank Tomitake Tsukihara for helpful advice and stimulating discussions at all stages of the x-ray crystallographic analysis and the members of beamline BL44XU for help during the data collection at SPring-8. This work was supported in part by Grant-in-Aid for Scientific Research in Priority Areas 18054011 from the Ministry of Education, Culture, Sports, Science, and Technology (Japan).

1. Hershko A, Ciechanover A, Varshavsky A (2000) *Nat Med* 6:1073–1081.
2. Sherman MY, Goldberg AL (2001) *Neuron* 29:15–32.
3. Pickart CM (2001) *Annu Rev Biochem* 70:503–533.
4. Deshaies RJ (1999) *Annu Rev Cell Dev Biol* 15:435–467.
5. Jin J, Cardozo T, Lovering RC, Elledge SJ, Pagano M, Harper JW (2004) *Genes Dev* 18:2573–2580.
6. Yoshida Y (2003) *J Biochem (Tokyo)* 134:183–190.
7. Wu G, Xu G, Schulman BA, Jeffrey PD, Harper JW, Pavletich NP (2003) *Mol Cell* 11:1445–1456.
8. Orlicky S, Tang X, Willems A, Tyers M, Sicheri F (2003) *Cell* 112:243–256.
9. Schulman BA, Carrano AC, Jeffrey PD, Bowen Z, Kinnucan ER, Finnin MS, Elledge SJ, Harper JW, Pagano M, Pavletich NP (2000) *Nature* 408:381–386.
10. Zheng N, Schulman BA, Song L, Miller JJ, Jeffrey PD, Wang P, Chu C, Koepp DM, Elledge SJ, Pagano M, *et al.* (2002) *Nature* 416:703–709.
11. Hao B, Zheng N, Schulman BA, Wu G, Miller JJ, Pagano M, Pavletich NP (2005) *Mol Cell* 20:9–19.
12. Ellgaard L, Helenius A (2003) *Nat Rev Mol Cell Biol* 4:181–191.
13. Erhardt JA, Hynicka W, DiBenedetto A, Shen N, Stone N, Paulson H, Pittman RN (1998) *J Biol Chem* 273:35222–35227.
14. Yoshida Y, Chiba T, Tokunaga F, Kawasaki H, Iwai K, Suzuki T, Ito Y, Matsuoka K, Yoshida M, Tanaka K, *et al.* (2002) *Nature* 418:438–442.
15. Yoshida Y, Tokunaga F, Chiba T, Iwai K, Tanaka K, Tai T (2003) *J Biol Chem* 278:43877–43884.
16. Yoshida Y, Adachi E, Fukiya K, Iwai K, Tanaka K (2005) *EMBO Rep* 6:239–244.
17. Mizushima T, Hirao T, Yoshida Y, Lee SJ, Chiba T, Iwai K, Yamaguchi Y, Kato K, Tsukihara T, Tanaka K (2004) *Nat Struct Mol Biol* 11:365–370.
18. Aravind L, Koonin EV (1999) *J Mol Biol* 285:1353–1361.
19. Liang CJ, Yamashita K, Kobata A (1980) *J Biochem (Tokyo)* 88:51–58.
20. Williams RL, Greene SM, McPherson A (1987) *J Biol Chem* 262:16020–16031.
21. Ko TP, Williams R, McPherson A (1996) *Acta Crystallogr D* 52:160–164.
22. Hagihara S, Totani K, Matsuo I, Ito Y (2005) *J Med Chem* 48:3126–3129.
23. Zheng N, Wang P, Jeffrey PD, Pavletich NP (2000) *Cell* 102:533–539.
24. Otwinowski Z, Minor W (1997) *Methods Enzymol* 276:307–326.
25. Bricogne G, Vonrhein C, Flensburg C, Schiltz M, Paciorek W (2003) *Acta Crystallogr D* 59:2023–2030.
26. Collaborative Computational Project 4 (1994) *Acta Crystallogr D* 50:760–763.
27. Vagin AA, Teplyakov A (1997) *J Appl Crystallogr* 30:1022–1025.
28. Emsley P, Cowtan K (2004) *Acta Crystallogr D* 60:2126–2132.
29. Murshudov GN, Vagin AA, Dodson EJ (1997) *Acta Crystallogr D* 53:240–255.
30. Kraulis PJ (1991) *J Appl Crystallogr* 24:946–950.
31. Merritt EA, Murphy ME (1994) *Acta Crystallogr D* 50:869–873.
32. Potterton E, McNicholas S, Krissinel E, Cowtan K, Noble M (2002) *Acta Crystallogr D* 58:1955–1957.

Reprint Series

Science

1 June 2007 | S10

AAAS

Regulation of CD8$^+$ T Cell Development by Thymus-Specific Proteasomes

Shigeo Murata,[1,2]* Katsuhiro Sasaki,[1] Toshihiko Kishimoto,[3,4] Shin-ichiro Niwa,[5] Hidemi Hayashi,[3,5] Yousuke Takahama,[6] Keiji Tanaka[1]

Proteasomes are responsible for generating peptides presented by the class I major histocompatibility complex (MHC) molecules of the immune system. Here, we report the identification of a previously unrecognized catalytic subunit called β5t. β5t is expressed exclusively in cortical thymic epithelial cells, which are responsible for the positive selection of developing thymocytes. Although the chymotrypsin-like activity of proteasomes is considered to be important for the production of peptides with high affinities for MHC class I clefts, incorporation of β5t into proteasomes in place of β5 or β5i selectively reduces this activity. We also found that β5t-deficient mice displayed defective development of CD8$^+$ T cells in the thymus. Our results suggest a key role for β5t in generating the MHC class I–restricted CD8$^+$ T cell repertoire during thymic selection.

Proteasomes are multicatalytic proteinase complexes that are responsible for regulated proteolysis in eukaryotic cells and essential for the generation of antigenic peptides presented by major histocompatibility complex (MHC) class I molecules of the immune system in jawed vertebrates (*1*). Proteolysis is conducted by 20*S* proteasomes, which are large complexes composed of 28 subunits arranged as a cylinder in four heteroheptameric rings: $\alpha_{1\text{-}7}$, $\beta_{1\text{-}7}$, $\beta_{1\text{-}7}$, and $\alpha_{1\text{-}7}$. Among these, the three subunits called β1, β2, and β5 perform the catalytic function. In vertebrates, three additional β1i, β2i, and β5i subunits are induced by interferon (IFN)–γ and are preferentially incorporated into proteasomes. These immunoproteasomes produce antigenic peptides more efficiently than do constitutive proteasomes, and they play an important role in the elimination of virus-infected and tumor cells by CD8$^+$ T cells (*2*).

During a search for proteasome-related genes in a genome database (www.ensembl.org), we found a previously unrecognized gene product with high homology to β subunits of 20*S* proteasomes. The gene encoding it is located adjacent to the gene for β5, and the gene product is encoded by a single exon in both human and mouse genomes (fig. S1A). Orthologous genes are found specifically in vertebrates, implying that this gene emerged synchronously with genes involved in adaptive immunity in evolution, as did the immunoproteasomes (*2*). The expression of this gene was biased toward the thymus in an expressed sequence tag database (UniGene Mm.32009). Multiple sequence alignments showed that its putative active-site threonine residue was preceded by a propeptide that ends with a glycine residue, a hallmark of active β subunits (*3*–*6*) (fig. S1B). The dendrogram and homologies among catalytic β subunits indicated its close relation with β5 and β5i (Fig. 1A and fig. S1C), and we therefore named this gene *β5t*, as a thymus-specific β5 family member. Northern blot analysis confirmed the exclusive transcription of β5t in the thymus (fig. S1D). Immunoblot analysis of various mouse organs, with the use of an antibody specific to β5t (anti-β5t), further confirmed that the expression was thymus-specific (Fig. 1B). In comparison, β5i was predominantly expressed in a broad range of immune tissues (including the thymus and spleen and to a lesser extent in lung and liver), and it further differed from the wide distribution of β5 (Fig. 1B).

We next examined how β5t is incorporated into proteasomes. Thymic extracts were immunoprecipitated with an antibody to the 20*S* proteasome (anti-20*S*), (cross-specific for all 20*S* proteasomes) and with anti-β5t. These antibodies immunodepleted 20*S* proteasomes and β5t, respectively (fig. S2A). Quantitative immunoblotting of α5, an invariable subunit of 20*S* proteasomes, revealed that ~20% of the 20*S* proteasomes in the thymus contain β5t (fig. S2B). β5 and β5i were barely detected in the β5t-containing proteasomes, indicating that β5t was incorporated into 20*S* proteasomes, in place of β5 or β5i (Fig. 1C). Moreover, the IFN-γ–inducible subunits β1i and β2i were preferentially incorporated into the β5t-containing proteasomes, in

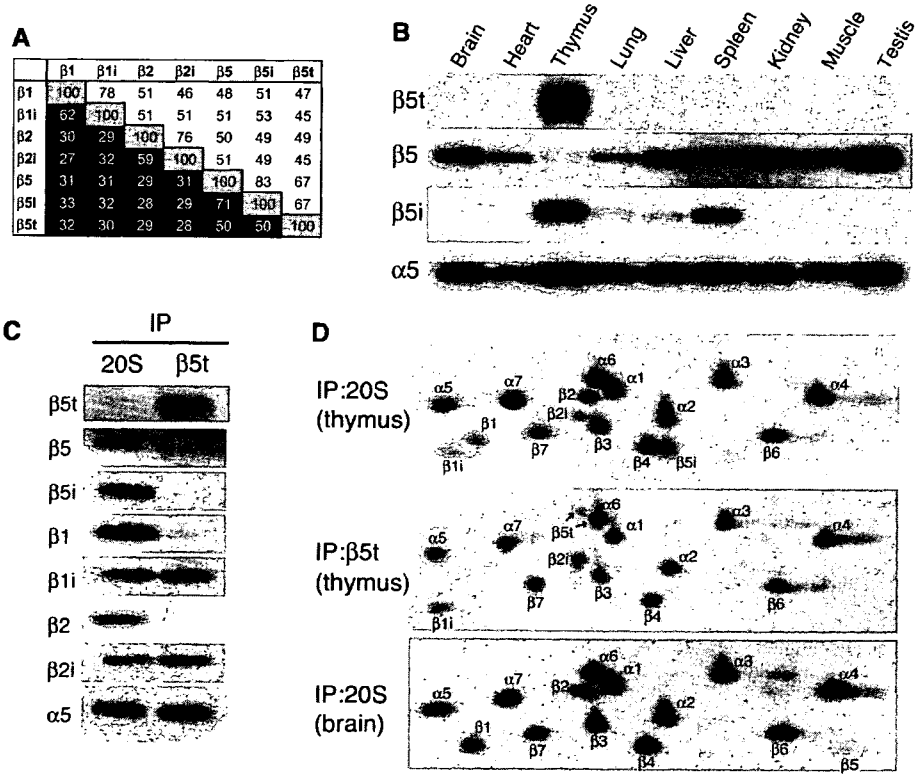

	β1	β1i	β2	β2i	β5	β5i	β5t
β1	100	78	51	46	48	51	47
β1i	62	100	51	51	51	53	45
β2	30	29	100	76	50	49	49
β2i	27	32	59	100	51	49	45
β5	31	31	29	31	100	83	67
β5i	33	32	28	29	71	100	67
β5t	32	30	29	28	50	50	100

Fig. 1. β5t is a catalytic proteasome subunit in the thymus. **(A)** Percentages of amino acid sequence identities (boxed in black) and similarities (white box) among primary structures of mouse catalytic subunits obtained with the BLAST2 program (*28*). **(B)** Immunoblot analysis of various tissues of 3-week-old mice with the indicated antibodies. **(C)** Extracts of mouse thymus were immunoprecipitated with anti-20*S* or anti-β5t, followed by immunoblotting with the indicated antibodies. IP, immunoprecipitation. **(D)** 2D-PAGE analysis of samples in (C) with Coomassie staining. 20*S* proteasomes of brain extracts represent constitutive proteasomes. All spots were identified by tandem mass spectrometry. One of the β5t spots (represented by arrows) overlaps with that of α6.

[1]Laboratory of Frontier Science, Core Technology and Research Center, Tokyo Metropolitan Institute of Medical Science, Bunkyo-ku, Tokyo 113-8613, Japan. [2]Precursory Research for Embryonic Science and Technology, Japan Science and Technology Agency, Kawaguchi, Saitama 332-0012, Japan. [3]Proteome Analysis Center, Faculty of Science, Toho University, Funabashi, Chiba 274-8510, Japan. [4]Department of Biomolecular Science, Faculty of Science, Toho University, Funabashi, Chiba 274-8510, Japan. [5]Link Genomics, Chuo-ku, Tokyo 103-0024, Japan. [6]Division of Experimental Immunology, Institute for Genome Research, Graduate School of Medical Science, University of Tokushima, Tokushima 770-8503, Japan.

*To whom correspondence should be addressed. E-mail: smurata@rinshoken.or.jp

place of constitutive subunits β1 and β2 (Fig. 1C). The above findings were further confirmed by analysis of the precipitated products by two-dimensional polyacrylamide gel electrophoresis (2D-PAGE) (Fig. 1D). Spots for β1, β2, β5, and β5i were faintly detected in the β5t-containing proteasomes, whereas spots for β5t emerged together with those for β1i and β2i (Fig. 1D, middle). We therefore propose to call this distinct subtype of proteasomes "thymoproteasomes."

Proteasomes are responsible for the production of MHC class I–binding peptides and the sole enzymes that determine the C termini of the peptides (*7*, *8*). Previous crystal structural studies of MHC class I complexes have revealed that the hydrophobic C-terminal anchor residues of the peptides are essential for high-affinity peptide binding into the clefts of MHC class I complexes (*9*). Some types of MHC molecules prefer basic C termini (*1*). The 20*S* proteasomes have at least three types of peptidase activities (chymotrypsin-like, trypsin-like, and caspase-like activities), which cleave peptide bonds after hydrophobic, basic, and acidic amino acids, respectively (*10*). The specificity is determined by the nature of the amino acids that compose the so-called S1 pocket (*11*, *12*). For the production of high-affinity MHC class I ligands, the chymotrypsin-like activity carried by β5 and β5i, whose S1 pockets are composed mostly of hydrophobic amino acids, is important (*13*). A comparison of the S1 pockets of the three β5 families revealed that the pocket of β5t is mainly composed of hydrophilic residues, in marked contrast to those of β5 and β5i (Fig. 2A), suggesting that thymoproteasomes have weaker chymotrypsin-like activity. To test this idea, we analyzed the peptidase activities of β5t-overexpressing cells, where ~90% of β5 was replaced by β5t (Fig. 2, B and C). We observed that the precursor forms of β5t were processed into mature forms after incorporation into 20*S* and 26*S* proteasomes (Fig. 2B, bottom left). In β5t-expressing cells, the chymotrypsin-like activity was exclusively reduced by 60 to 70%, without affecting the other two activities in both 20*S* and 26*S* fractions (Fig. 2B). Kinetic analysis of the chymotrypsin-like activity revealed that β5t reduced both the maximum velocity and the Michaelis constant values for the activity (Fig. 2D), which is opposite to the effect that β5i has on these quantities (*14*). However, these cells still possessed normal protein-degrading activity, as assessed by the

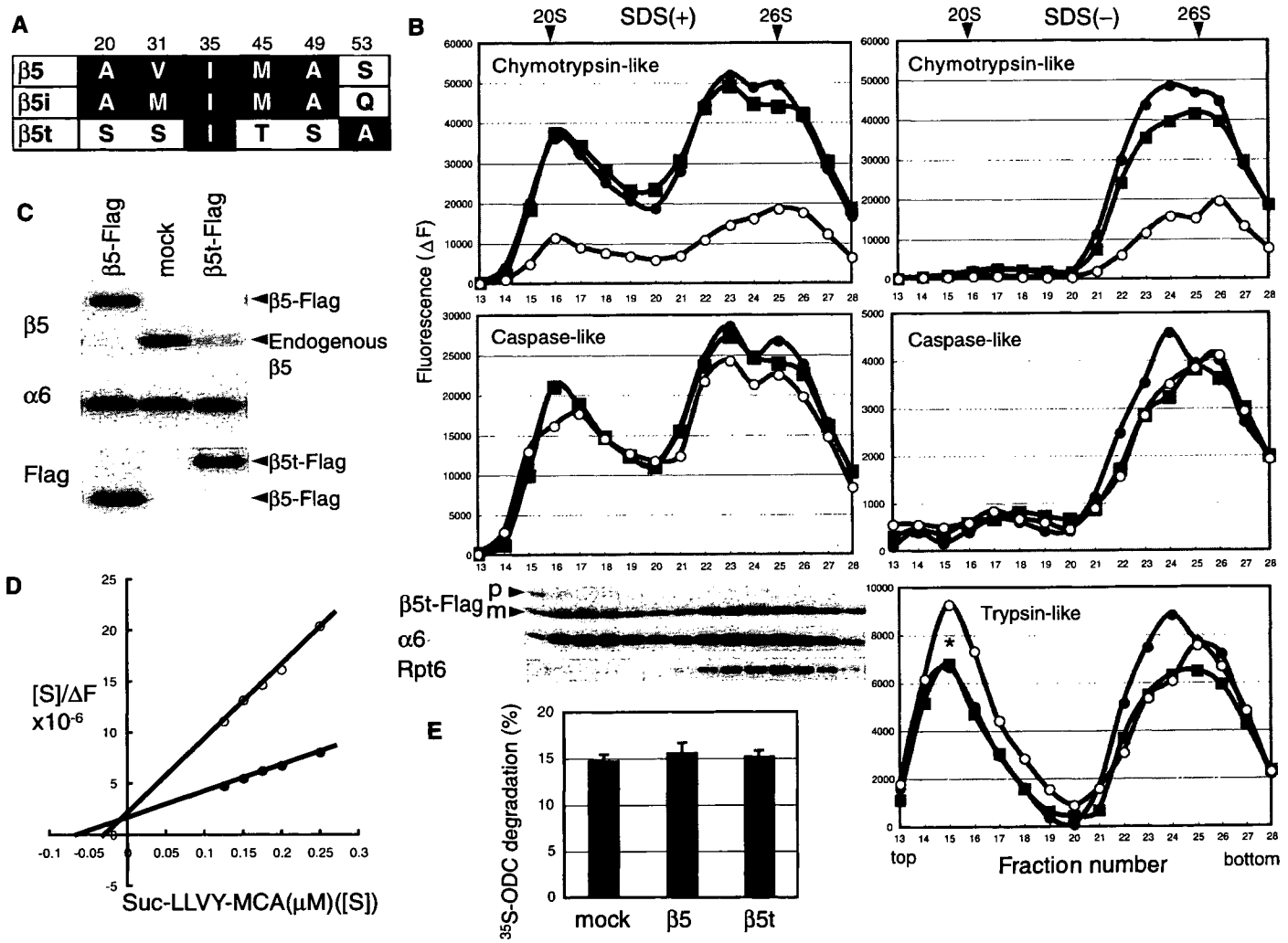

Fig. 2. β5t selectively reduces the chymotrypsin-like activity of proteasomes. **(A)** Alignment of amino acid residues organizing the S1 pockets of β5 families. The hydrophobic and hydrophilic amino acid residues are boxed in black and white, respectively. The numbers represent the position from the active-site threonine. **(B)** Peptidase activities of human embryonic kidney–293 T cells expressing human β5t-Flag (open circles), β5-Flag (black squares), or mock cells (black circles) in the presence (left) and absence (right) of 0.025% SDS. Arrowheads indicate the peak locations of 20*S* proteasomes and 26*S* proteasomes, proven by immunoblot analysis of each fraction (bottom left). p, precursor; m, mature; asterisk, nonproteasomal activity. **(C)** Fraction numbers 25 in (B) were immunoblotted for β5, α6, and Flag. **(D)** Hanes-Woolf plots for chymotrypsin-like activity of 26*S* proteasomes (pools of fraction numbers 24 to 26) from mock cells (black circles) and β5t cells (open circles). Suc-LLVY-MCA, succinyl-Leu-Leu-Val-Tyr-4-methylcoumaryl-7-amide; [S], substrate concentration. **(E)** Cell extracts from (B) were assayed for adenosine triphosphate–dependent protein degradation activity using ^{35}S-labeled ODC. Mean ± SD; $n = 3$ experiments.

degradation of ornithine decarboxylase (ODC) (Fig. 2E) (*15*).

The thymus is responsible for generating a T cell repertoire that specifically recognizes self-peptide–MHC (self-pMHC) complexes and tolerates self-antigens. Thymic stromal cells represent a heterogeneous mixture of cell types and provide a proper microenvironment for developing thymocytes (*16*, *17*). To identify a cell type that expresses β5t, we immunostained sections of mouse thymus for β5t and markers for thymic stromal cells (Fig. 3, A and B). β5t was exclusively expressed in the thymic cortex, which is quite similar to the expression of Ly51, a marker for cortical thymic epithelial cells (cTECs). The distribution of β5t was distinct from that of cells that bind to *Ulex europaeus* agglutinin I (UEA-I), a marker for medullary TECs; CD11c, a marker for dendritic cells; and MTS15, a marker for fibroblasts (Fig. 3A) (*18*–*20*). A magnified image of the cortex revealed that the reticular staining pattern of β5t is nearly identical to that of Ly51, indicating that β5t is exclusively expressed in cTECs (Fig. 3B).

To confirm this conclusion, different cell populations of the thymus were isolated. Immunoblot analysis demonstrated that β5t is specifically expressed in Ly51-positive cells and is not detected in any other stromal cells or in $CD45^+$ cells that are mostly composed of thymocytes (Fig. 3C). A comparison of Ly51-positive cells with murine embryonic fibroblasts that were treated with or without IFN-γ [in which almost all the proteasomes are immuno- and constitutive proteasomes, respectively (*21*)] revealed that the majority of proteasomes in cTECs were thymoproteasomes containing β5t, together with β1i and β2i. Also, the expression levels of β5 and β5i were markedly down-regulated in cTECs (Fig. 3D).

To clarify the physiological role of β5t, we generated β5t-deficient mice. The β5t-coding sequence was substituted for cDNA encoding the protein Venus to identify β5t-expressing cells (Fig. 4A). The loss of β5t proteins in the $\beta5t^{-/-}$ thymus and the expression of Venus in the $\beta5t^{-/-}$ and $\beta5t^{+/-}$ thymuses were confirmed by immunoblotting (Fig. 4B). An inspection of $\beta5t^{+/-}$ and $\beta5t^{-/-}$ mice with fluorescence demonstrated that the expression of Venus (i.e., β5t) was limited to the cortex of the thymus with a reticular pattern similar to that of cTECs (fig. S3, A to C). Cortical and medullary architectures, as well as the size of the thymuses of $\beta5t^{-/-}$ mice, were indistinguishable from those of $\beta5t^{+/-}$ mice (fig. S3, B and C). When thymic stromal cells from $\beta5t^{+/-}$ mice were analyzed by flow cytometry, all Venus-expressing cells were MHC class II $I\text{-}A^b$–positive (Fig. 4C). Furthermore, we examined the relationship between Venus and Ly51 expression in the $I\text{-}A^b$–positive population (Fig. 4D). We identified three distinct populations. Among them, the $Venus^+Ly51^+$ population was the largest, constituting 50% of $I\text{-}A^b$–positive cells. There was a smaller population of $Venus^-Ly51^+$ that constituted 11% of $I\text{-}A^b$–positive cells. These results demonstrate that all β5t-expressing cells are $I\text{-}A^{b+}Ly51^+$ cTECs and that this population makes up ~80% of cTECs.

It has been suggested that cTECs are mainly responsible for positive selection by presenting ligands on MHC molecules to $CD4^+CD8^+$ double-positive (DP) thymocytes (*22*–*25*). We therefore examined how β5t is involved in the function of cTECs. Flow cytometry analysis of thymocytes revealed that β5t deficiency was associated with a markedly low percentage of CD8 single-positive (SP) thymocytes but not with the percentage of CD4 SP thymocytes (Fig. 4E). A large proportion (80.7%) of wild-type (WT) CD8 SP thymocytes expressed high levels of T cell receptor β (TCRβ), resembling positively selected cells (Fig. 4F, left) (*26*). In contrast, a much smaller proportion (50.2%) of CD8 SP thymocytes expressed high levels of TCRβ in $\beta5t^{-/-}$ mice (Fig. 4F, right), suggesting that many of the CD8 SP thymocytes of $\beta5t^{-/-}$ mice are immature thymocytes that are transitory intermediates between double-negative (DN) and DP thymocytes (*27*). Consequently, the ratio of CD4 SP cells to CD8 SP cells in $\beta5t^{-/-}$ mice was markedly higher than that in WT mice (Fig. 4G). The ratio was also significantly elevated in $\beta5t^{+/-}$ mice, although the difference was much smaller (Fig. 4G). Total numbers of DN, DP, and CD4 SP thymocytes in $\beta5t^{-/-}$ mice were nearly identical to those of $\beta5t^{+/-}$ and WT mice. However, a significantly low total number of CD8 SP thymocytes was observed in $\beta5t^{-/-}$ mice (Fig. 4H). Selective reduction of CD8 SP T cells was also observed in TCRβ(+) splenocytes of $\beta5t^{-/-}$ mice

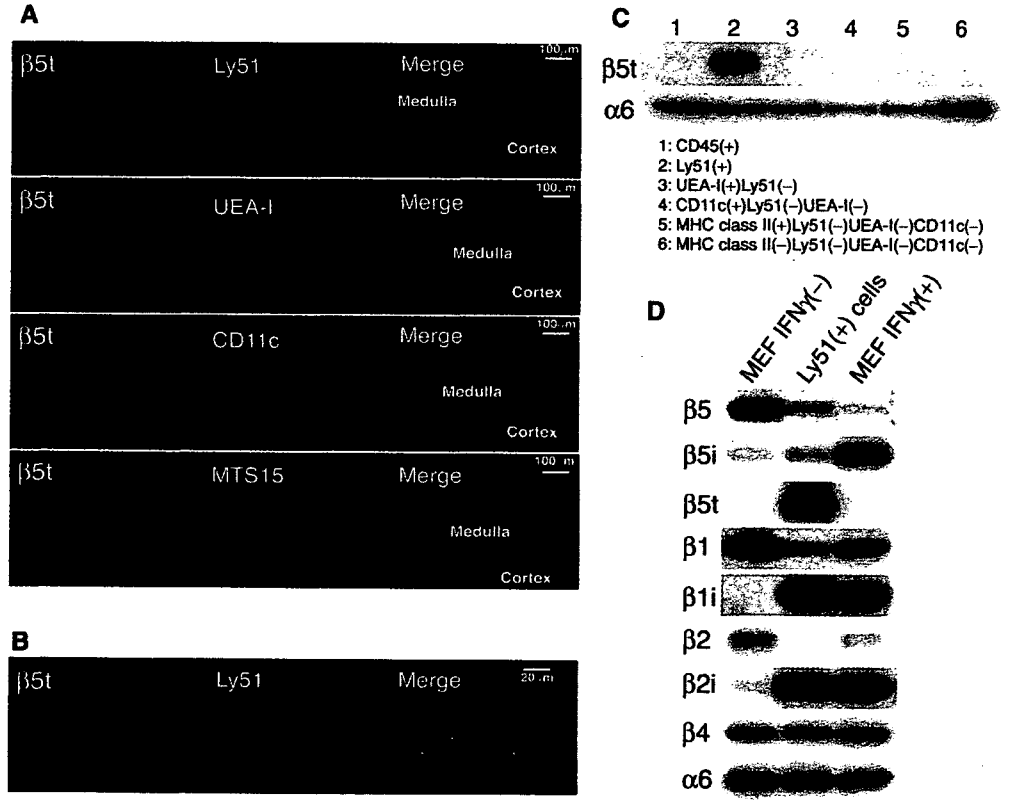

Fig. 3. β5t is specifically expressed in cTECs. (**A** and **B**) Cryosections of mouse thymus were immunostained for β5t, together with Ly51, UEA-I, CD11c, or MTS15. (**C**) Various populations of cells from the thymus were immunoblotted for β5t and α6 (a loading control for proteasomes). (**D**) Contents of thymoproteasomes in Ly51-positive cells were analyzed by immunoblotting. MEF, murine embryonic fibroblast.

(Fig. 4, I and J). These results demonstrate that β5t is required for the development of $CD8^+$ T cells in the thymus and suggest the possibility that β5t deficiency is associated with defective positive selection of $CD8^+$ T cells.

During positive selection, DP cells that interact with self-pMHC complexes expressed on cTECs with sufficiently low affinity or avidity are rescued from intrathymic death and induced to differentiate into CD4 or CD8 SP thymocytes. The recognition of MHC class I molecules results in commitment to the CD8 lineage (*22–26*). In contrast, DP cells that interact with high affinity or avidity with self-pMHC complexes are eliminated by the induction of apoptosis (*22–24*). To date, however, information about whether and how cTECs can offer specialized signals that are suitable for positive selection has been elusive. The present work demonstrates that β5t, which is specifically expressed in cTECs, plays a pivotal role in the development of $CD8^+$ T cells. What, then, is the mechanism for $CD8^+$ T cell development regulated by β5t? The thymic architecture was apparently normal in $\beta5t^{-/-}$ mice (fig. S3, B and C), suggesting that β5t is not essential for the differentiation and proliferation of cTECs. Normal development of CD4 SP thymocytes observed in $\beta5t^{-/-}$ mice supports this argument. Surface expression levels of MHC class I on $\beta5t^{-/-}$ cTECs were also comparable to those of $\beta5t^{+/-}$ cTECs (fig. S4). It is assumed that other β5 family members (e.g., β5 and β5i subunits) are incorporated in place of β5t in cTECs of

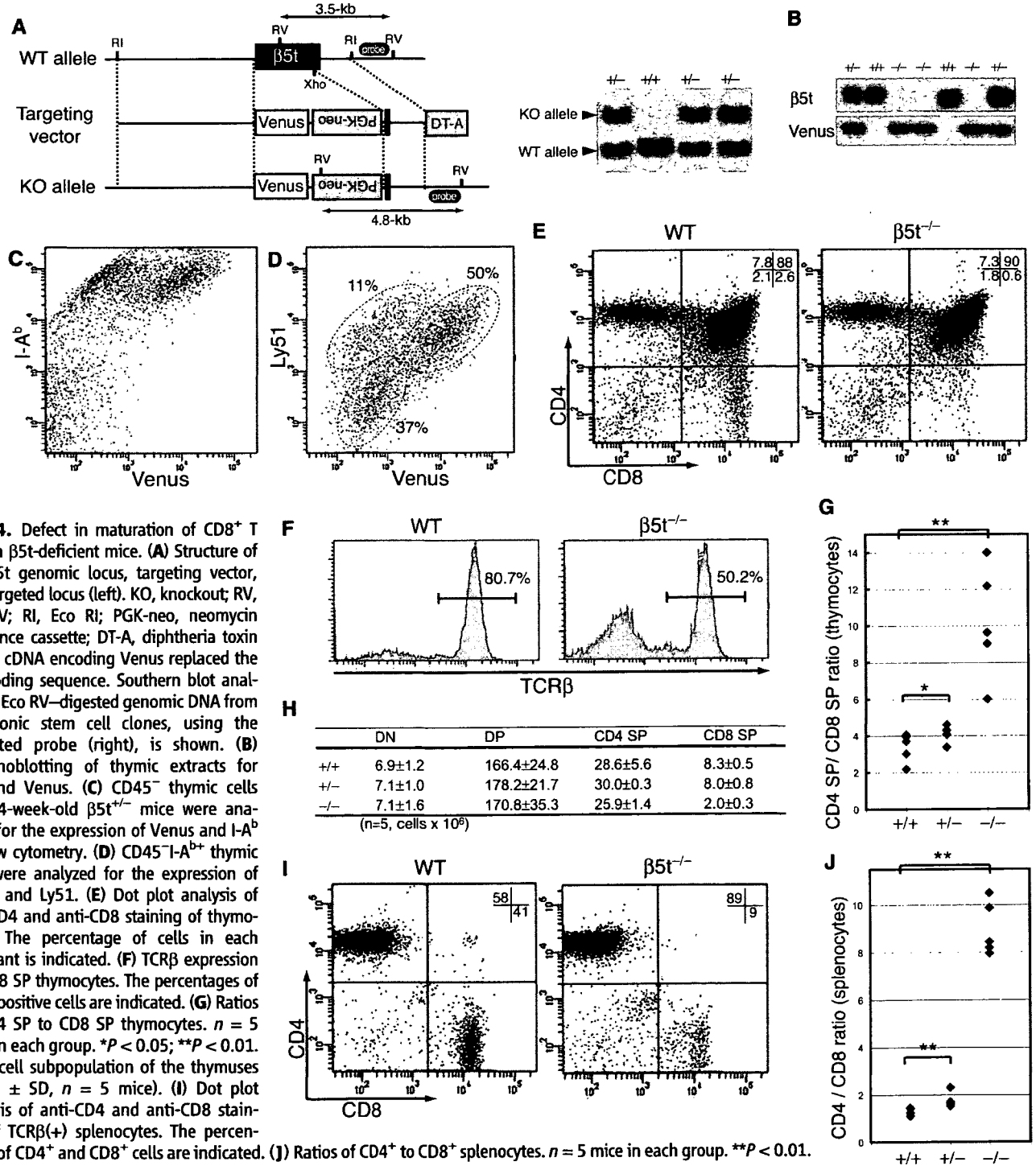

Fig. 4. Defect in maturation of $CD8^+$ T cells in β5t-deficient mice. **(A)** Structure of the β5t genomic locus, targeting vector, and targeted locus (left). KO, knockout; RV, Eco RV; RI, Eco RI; PGK-neo, neomycin resistance cassette; DT-A, diphtheria toxin A. The cDNA encoding Venus replaced the β5t coding sequence. Southern blot analysis of Eco RV–digested genomic DNA from embryonic stem cell clones, using the indicated probe (right), is shown. **(B)** Immunoblotting of thymic extracts for β5t and Venus. **(C)** $CD45^-$ thymic cells from 4-week-old $\beta5t^{+/-}$ mice were analyzed for the expression of Venus and $I\text{-}A^b$ by flow cytometry. **(D)** $CD45^-I\text{-}A^{b+}$ thymic cells were analyzed for the expression of Venus and Ly51. **(E)** Dot plot analysis of anti-CD4 and anti-CD8 staining of thymocytes. The percentage of cells in each quadrant is indicated. **(F)** TCRβ expression on CD8 SP thymocytes. The percentages of TCRβ-positive cells are indicated. **(G)** Ratios of CD4 SP to CD8 SP thymocytes. $n = 5$ mice in each group. $^*P < 0.05$; $^{**}P < 0.01$. **(H)** T cell subpopulation of the thymuses (mean ± SD, $n = 5$ mice). **(I)** Dot plot analysis of anti-CD4 and anti-CD8 staining of TCRβ(+) splenocytes. The percentages of $CD4^+$ and $CD8^+$ cells are indicated. **(J)** Ratios of $CD4^+$ to $CD8^+$ splenocytes. $n = 5$ mice in each group. $^{**}P < 0.01$.

$\beta5t^{-/-}$ mice. Considering that proteasomes are essential for the production of MHC class I ligands and that β5t specifically attenuates the peptidase activities that cleave peptide bonds after hydrophobic amino acid residues, it is possible that thymoproteasomes predominantly produce low-affinity MHC class I ligands rather than high-affinity ligands in cTECs, as compared with constitutive- and immunoproteasomes, thereby supporting positive selection.

References and Notes

1. K. L. Rock, A. L. Goldberg, *Annu. Rev. Immunol.* **17**, 739 (1999).
2. K. Tanaka, M. Kasahara, *Immunol. Rev.* **163**, 161 (1998).
3. E. Seemuller *et al.*, *Science* **268**, 579 (1995).
4. P. Chen, M. Hochstrasser, *Cell* **86**, 961 (1996).
5. G. Schmidtke *et al.*, *EMBO J.* **15**, 6887 (1996).
6. Materials and methods are available as supporting material on *Science* Online.
7. K. L. Rock, I. A. York, A. L. Goldberg, *Nat. Immunol.* **5**, 670 (2004).
8. P. Cascio, C. Hilton, A. F. Kisselev, K. L. Rock, A. L. Goldberg, *EMBO J.* **20**, 2357 (2001).
9. A. C. Young, S. G. Nathenson, J. C. Sacchettini, *FASEB J.* **9**, 26 (1995).
10. O. Coux, K. Tanaka, A. L. Goldberg, *Annu. Rev. Biochem.* **65**, 801 (1996).
11. M. Groll *et al.*, *Nature* **386**, 463 (1997).
12. M. Unno *et al.*, *Structure* **10**, 609 (2002).
13. H. J. Fehling *et al.*, *Science* **265**, 1234 (1994).
14. M. Gaczynska, K. L. Rock, T. Spies, A. L. Goldberg, *Proc. Natl. Acad. Sci. U.S.A.* **91**, 9213 (1994).
15. A. F. Kisselev, A. Callard, A. L. Goldberg, *J. Biol. Chem.* **281**, 8582 (2006).
16. A. W. Goldrath, M. J. Bevan, *Nature* **402**, 255 (1999).
17. T. K. Starr, S. C. Jameson, K. A. Hogquist, *Annu. Rev. Immunol.* **21**, 139 (2003).
18. D. H. Gray, A. P. Chidgey, R. L. Boyd, *J. Immunol. Methods* **260**, 15 (2002).
19. J. Gill, M. Malin, G. A. Hollander, R. Boyd, *Nat. Immunol.* **3**, 635 (2002).
20. T. Akiyama *et al.*, *Science* **308**, 248 (2005).
21. S. Murata *et al.*, *EMBO J.* **20**, 5898 (2001).
22. G. Anderson, E. J. Jenkinson, *Nat. Rev. Immunol.* **1**, 31 (2001).
23. H. von Boehmer *et al.*, *Immunol. Rev.* **191**, 62 (2003).
24. K. A. Hogquist, T. A. Baldwin, S. C. Jameson, *Nat. Rev. Immunol.* **5**, 772 (2005).
25. B. H. Koller, P. Marrack, J. W. Kappler, O. Smithies, *Science* **248**, 1227 (1990).
26. H. von Boehmer, *Cell* **76**, 219 (1994).
27. H. R. Macdonald *et al.*, *Eur. J. Immunol.* **18**, 519 (1988).
28. The BLAST2 program, www.ncbi.nlm.nih.gov/blast/bl2seq/wblast2.cgi.

29. We thank K. Furuyama for technical support and M. Kasahara for discussion. This work was supported by grants from the Japan Science and Technology Agency (S.M.) and the Ministry of Education, Science and Culture of Japan (S.M. and K.T.). The accession numbers for mouse and human β5t are AB299436 and AB299437, respectively, in the DNA Data Bank of Japan.

Supporting Online Material

www.sciencemag.org/cgi/content/full/316/5829/1349/DC1
Materials and Methods
Figs. S1 to S4
References

28 February 2007; accepted 13 April 2007
10.1126/science.1141915

Essential role for autophagy protein Atg7 in the maintenance of axonal homeostasis and the prevention of axonal degeneration

Masaaki Komatsu*†‡, Qing Jun Wang§¶, Gay R. Holstein¶, Victor L. Friedrich, Jr.¶, Jun-ichi Iwata*†, Eiki Kominami†, Brian T. Chait§, Keiji Tanaka*, and Zhenyu Yue¶‖

¶Departments of Neurology and Neuroscience, Mount Sinai School of Medicine, New York, NY 10029; *Laboratory of Frontier Science, Tokyo Metropolitan Institute of Medical Science, Bunkyo-ku, Tokyo 113-8613, Japan; †Department of Biochemistry, Juntendo University School of Medicine, Bunkyo-ku, Tokyo 113-8421, Japan; ‡Precursory Research for Embryonic Science and Technology, Japan Science and Technology Corporation, Kawaguchi 332-0012, Japan; and §Laboratory of Mass Spectrometry and Gaseous Ion Chemistry, Rockefeller University, New York, NY 10065

Edited by Pietro V. De Camilli, Yale University School of Medicine, New Haven, CT, and approved July 19, 2007 (received for review February 14, 2007)

Autophagy is a regulated lysosomal degradation process that involves autophagosome formation and transport. Although recent evidence indicates that basal levels of autophagy protect against neurodegeneration, the exact mechanism whereby this occurs is not known. By using conditional knockout mutant mice, we report that neuronal autophagy is particularly important for the maintenance of local homeostasis of axon terminals and protection against axonal degeneration. We show that specific ablation of an essential autophagy gene, *Atg7*, in Purkinje cells initially causes cell-autonomous, progressive dystrophy (manifested by axonal swellings) and degeneration of the axon terminals. Consistent with suppression of autophagy, no autophagosomes are observed in these dystrophic swellings, which is in contrast to accumulation of autophagosomes in the axonal dystrophic swellings under pathological conditions. Axonal dystrophy of mutant Purkinje cells proceeds with little sign of dendritic or spine atrophy, indicating that axon terminals are much more vulnerable to autophagy impairment than dendrites. This early pathological event in the axons is followed by cell-autonomous Purkinje cell death and mouse behavioral deficits. Furthermore, ultrastructural analyses of mutant Purkinje cells reveal an accumulation of aberrant membrane structures in the axonal dystrophic swellings. Finally, we observe double-membrane vacuole-like structures in wild-type Purkinje cell axons, whereas these structures are abolished in mutant Purkinje cell axons. Thus, we conclude that the autophagy protein Atg7 is required for membrane trafficking and turnover in the axons. Our study implicates impairment of axonal autophagy as a possible mechanism for axonopathy associated with neurodegeneration.

axon | axonopathy | neurodegeneration | autophagosome | Purkinje cell

Macroautophagy is characterized by dynamic membrane rearrangements, involving the formation, trafficking, and degradation of double-membrane autophagic vacuoles (autophagosomes) in the cytoplasm. Macroautophagy (hereafter referred to as autophagy) is a highly regulated process, which can be induced by nutrient starvation, trophic factors, and stress (1). Despite recent advances in characterizing autophagy in several model systems, autophagic processes in the nervous system remain poorly understood. On one hand, nutrient deprivation has not been observed to induce autophagy in the mammalian brain (2), thus suggesting a specific regulatory system for autophagy that is not typically activated by starvation. On the other hand, a variety of conditions that cause neuronal stress or degeneration can lead to the accumulation of autophagosomes in neurons, thus implicating autophagy in these neuropathogenic processes (3, 4).

The axon is a highly specialized neuronal compartment that performs many functions independently from the cell body. After axotomy or excitotoxicity, double-membrane vacuoles resembling autophagosomes were originally observed to accumulate in dilated axon terminals that result from the injury (5, 6), a local phenomenon that is not observed in undisturbed axons. Autophagosome-like vacuoles have also been shown to be present in the dysfunctional or degenerating axons associated with a range of chronic neurodegenerative conditions, including Alzheimer's (7, 8), Parkinson's (9), Huntington's (10), and Creutzfeldt–Jakob (11) diseases and their animal models (12–14). These observations suggest a link between locally altered autophagy and axonopathy, which is one of the underlying mechanisms in neurodegeneration (15).

Although the biological significance of these autophagosomes-like vacuoles in degenerating axons is unclear, recent studies have shown that genetic inactivation of autophagy in the mouse CNS causes neurodegeneration accompanied by axonal dystrophy and the formation of intracellular ubiquitin-associated inclusions (16, 17). These studies suggest a role for basal levels of autophagy in neuronal protection and in protein quality control. However, the connection between the inactivation of autophagy and the observed axonal dystrophy and neurodegeneration remains to be determined. In addition, because autophagy was suppressed in all cell types in the CNS (including neurons and nonneuronal cells) (16, 17), it is not known whether the observed axonal dystrophy and neurodegeneration is cell-autonomous.

Here, we seek to further elucidate the physiological function of neuronal autophagy by generating conditional knockout mice with Purkinje cell-specific deletion of *Atg7*, an autophagy gene encoding E1-like enzyme in the two ubiquitin-like conjugation systems that are essential for the autophagosome biogenesis (18). We show that ablation of Atg7 leads to abnormal swellings and dystrophy of Purkinje cell axon terminals in the deep cerebellar nuclei (DCN). Subsequently, these *Atg7*-deletion mice develop cell-autonomous neurodegeneration of Purkinje cells, dendritic atrophy, and behavioral deficits. Moreover, double-membrane vacuole-like structures are formed in the distal ends of wild-type Purkinje cell axons, whereas they are absent in *Atg7*-deletion Purkinje cell axons.

Author contributions: M.K. and Q.J.W. contributed equally to this work; M.K., Q.J.W., and Z.Y. designed research; M.K., Q.J.W., G.R.H., and J.-i.I. performed research; M.K., Q.J.W., G.R.H., V.L.F., J.-i.I., E.K., B.T.C., K.T., and Z.Y. analyzed data; and Q.J.W., B.T.C., and Z.Y. wrote the paper.

The authors declare no conflict of interest.

This article is a PNAS Direct Submission.

Abbreviations: DCN, deep cerebellar nucleus; P*n*, postnatal day *n*; LC3, light chain 3; mGluR, metabotropic glutamate receptor.

‖To whom correspondence should be addressed at: Department of Neurology, Mount Sinai School of Medicine, Box 1137, Annenberg 14-62, One Gustave L. Levy Place, New York, NY 10029. E-mail: zhenyu.yue@mssm.edu.

This article contains supporting information online at www.pnas.org/cgi/content/full/0701311104/DC1.

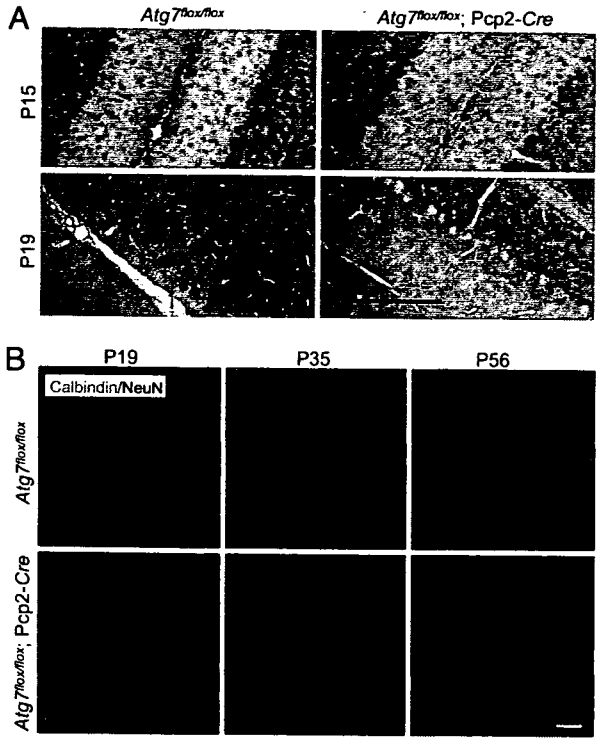

Fig. 1. Deletion of *Atg7* specifically in Purkinje cells caused progressive dystrophic swelling of axon terminals. (*A*) Immunohistochemistry of Atg7 protein expression in Purkinje cells of *Atg7*$^{flox/flox}$ and *Atg7*$^{flox/flox}$;Pcp2-*Cre* mice at P15 and P19. The endogenous Atg7 protein was present at P15 but absent at P19 in the *Atg7*$^{flox/flox}$;Pcp2-*Cre* Purkinje cells. (Scale bar: 100 μm.) (*B*) Progression of the abnormal Purkinje cell axon terminal swellings in the DCN of *Atg7*$^{flox/flox}$;Pcp2-*Cre* mice (anti-calbindin immunofluorescent staining in green with anti-NeuN counterstained in red) at P19, P35, and P56. *Atg7*$^{flox/flox}$ was used as control. (Scale bar: 20 μm.) n = 3–5.

Instead, the mutant Purkinje cell axon terminal swellings accumulate aberrant membranous structures. Our results suggest that autophagy is required for normal axon terminal membrane trafficking and turnover, and indicate an essential role of local autophagy in the maintenance of axonal homeostasis and prevention of axonal degeneration.

Results

Specific Depletion of Atg7 in Purkinje Cells Caused Cell-Autonomous Dystrophy and Degeneration of Axon Terminals. To generate Purkinje cell-specific deletion of *Atg7* in mice, we crossed mice harboring the floxed *Atg7* alleles (19) with transgenic mice expressing *Cre* recombinase under control of the Pcp2 (L7) promoter (20) to establish the mouse line *Atg7*$^{flox/flox}$;Pcp2-*Cre*. To determine when loss of the endogenous Atg7 protein occurred, we examined Atg7 expression in *Atg7*$^{flox/flox}$;Pcp2-*Cre* mice at postnatal day 15 (P15) and P19. At P15, Atg7 was expressed at similar levels in Purkinje cells of both mutant *Atg7*$^{flox/flox}$;Pcp2-*Cre* and the control *Atg7*$^{flox/flox}$ mice, whereas at P19, despite residual expression in a small number of Purkinje cells (<12%), Atg7 immunostaining was largely diminished in *Atg7*$^{flox/flox}$;Pcp2-*Cre* Purkinje cells (>88%), but unchanged in the *Atg7*$^{flox/flox}$ Purkinje cells (Fig. 1*A*). At P35, >95% Purkinje cells in *Atg7*$^{flox/flox}$;Pcp2-*Cre* showed no detectable Atg7 expression (data not shown). In addition, Atg7 deficiency in *Atg7*$^{flox/flox}$;Pcp2-*Cre* mice was specific for Purkinje cells because Atg7 is clearly present in the other cell types (Fig. 1*A*). Thus, the specific loss of Atg7 in Purkinje cells occurred largely between P15 and P19 in *Atg7*$^{flox/flox}$;Pcp2-*Cre* mice.

Next, we examined Purkinje cell axons in the DCN of *Atg7*$^{flox/flox}$;Pcp2-*Cre* mice by immunofluorescent staining using an antibody against calbindin, a Purkinje cell marker. At P15, no morphological alteration was observed in the axons of *Atg7*$^{flox/flox}$;Pcp2-*Cre* Purkinje cells compared with those of *Atg7*$^{flox/flox}$ Purkinje cells [supporting information (SI) Fig. 7], consistent with the presence of normal levels of Atg7 in *Atg7*$^{flox/flox}$;Pcp2-*Cre* Purkinje cells at this stage (Fig. 1*A*). However, at P19, *Atg7*$^{flox/flox}$;Pcp2-*Cre* Purkinje cell axons were abnormally dilated, as visualized by green fluorescence-labeled "endbulbs" (Fig. 1*B*). In addition, these Purkinje cell axonal swellings were labeled with the antibody raised against synaptophysin, the presynaptic terminal marker (SI Fig. 8), suggesting that they were terminals of Purkinje cell axons. The number and size of the swollen axon terminals in the DCN of the *Atg7*$^{flox/flox}$;Pcp2-*Cre* were markedly increased at P35 in comparison with those at P19 (Fig. 1*B*). At P56, the number of such axonal dystrophic swellings of the mutant Purkinje cells was noticeably decreased in comparison with that at P35, suggesting that many of these swollen axons had degenerated by this age (Fig. 1*B*). These data demonstrated that deletion of *Atg7* caused cell-autonomous axonal dystrophy and degeneration in Purkinje cells.

Axonal Dystrophic Swellings of *Atg7*$^{flox/flox}$;Pcp2-*Cre* Purkinje Cells Were Devoid of GFP-Light Chain 3 (LC3)-Labeled Puncta and Exhibited Increased Levels of p62/SQSTM1. Transgenic mice producing GFP fused with microtubule-associated protein 1 light chain 3 (LC3), a specific marker for autophagosomes (21), were previously generated to monitor autophagosomes *in vivo* (2). By expressing GFP-LC3 in *Lurcher* mice (GFP-LC3/*Lurcher*), we showed that a large number of autophagosomes were formed in the dystrophic axon terminals of *Lurcher* Purkinje cells (Fig. 2*Ad*), providing *in vivo* evidence for the induction of autophagy in response to *Lurcher*-induced excitotoxicity (22). To assess autophagic activity in the dystrophic axons of *Atg7*$^{flox/flox}$;Pcp2-*Cre* Purkinje cells, we crossed transgenic GFP-LC3 with *Atg7*$^{flox/flox}$;Pcp2-*Cre* mice (*Atg7*$^{flox/flox}$;Pcp2-*Cre*/GFP-LC3). Despite intense GFP-LC3 accumulation in the axonal dystrophic swellings of Purkinje cells in *Atg7*$^{flox/flox}$;Pcp2-*Cre*/GFP-LC3 mice at P35, no GFP-LC3 fluorescent puncta characteristic of autophagosomes were observed in these swellings (Fig. 2*A b* and *c*). We contrasted this finding to our observation of GFP-LC3 puncta in Purkinje cell axons GFP-LC3/*Lurcher* mice (Fig. 2*Ad*) (22). In addition, no GFP-LC3 puncta were observed in the somata or dendrites of *Atg7*$^{flox/flox}$;Pcp2-*Cre*/GFP-LC3 Purkinje cells (Fig. 2*A f* and *g*), again in contrast to the observation of GFP-LC3 puncta in the somata and dendrites of GFP-LC3/*Lurcher* Purkinje cells (Fig. 2*Ah*) (22).

It has been shown that inhibition of autophagy is correlated with increased levels of the polyubiquitin binding protein p62/SQSTM1 (22, 23). We thus examined the levels of p62/SQSTM1 in *Atg7*$^{flox/flox}$;Pcp2-*Cre* Purkinje cells. As detected with anti-p62/SQSTM1 immunofluorescent staining, p62/SQSTM1 was markedly accumulated in the axonal dystrophic swellings (Fig. 2*B*, arrows) and somata (SI Fig. 9) of *Atg7*$^{flox/flox}$;Pcp2-*Cre* Purkinje cells in comparison with *Atg7*$^{flox/flox}$ Purkinje cells. It is also noteworthy that the dystrophic axonal swellings in *Lurcher* Purkinje cells did not have detectable p62/SQSTM1 immunofluorescent staining (SI Fig. 10). These results provided molecular evidence for impaired autophagic activity in the dystrophic axons of *Atg7*$^{flox/flox}$;Pcp2-*Cre* Purkinje cells, but not in the dystrophic axons of *Lurcher* Purkinje cells.

***Atg7*$^{flox/flox}$;Pcp2-*Cre* Purkinje Cells Exhibited Normal Dendritic Tree and Spine Morphology at P56.** Despite the remarkable dystrophy and degeneration of Purkinje cell axon terminals in the DCN of *Atg7*$^{flox/flox}$;Pcp2-*Cre* mice at P35 and P56, the cerebellar cortex displayed little change in its overall size and organization (Fig. 3*A*). For example, at P35 and P56, *Atg7*$^{flox/flox}$;Pcp2-*Cre* mice and

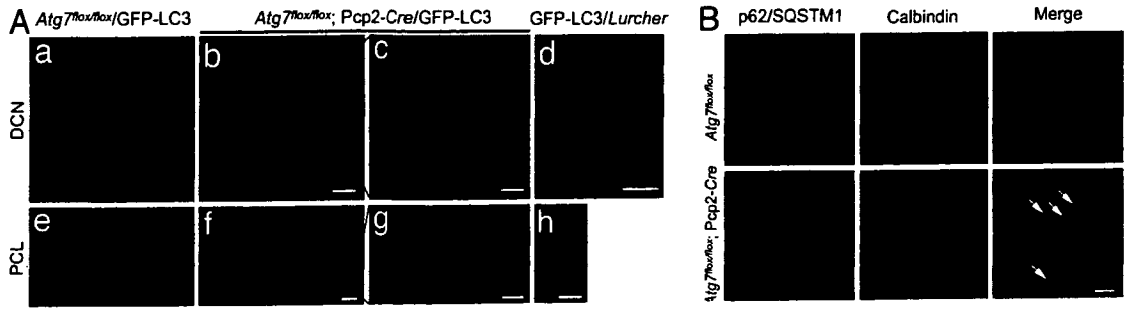

Fig. 2. The axonal dystrophic swellings of the *Atg7*-deficient Purkinje cells contained no GFP-LC3 labeled autophagosomes but accumulated p62/SQSTM1. (*A*) The absence of GFP-LC3 puncta in Purkinje cell axonal dystrophic swellings (*b* and *c*) and somata (*f* and *g*) of *Atg7*$^{flox/flox}$;Pcp2-*Cre*/GFP-LC3 mice (P35). GFP-LC3 puncta were found in GFP-LC3/*Lurcher* Purkinje cell axonal dystrophic swellings (*d*) and somata (*h*) (P12). DCN (*a*) and Purkinje cell layer (PCL) (*e*) of control mice Atg7$^{flox/flox}$/GFP-LC3 are shown. (Scale bars: *a*, *b*, *e*, and *f*, 20 μm; *c*, *d*, *g*, and *h*, 10 μm.) (*B*) Anti-p62/SQSTM1 immunofluorescent staining (in green) showed accumulation of p62/SQSTM1 in Purkinje cell axonal dystrophic swellings (calbindin labeling in red) (white arrows) in the DCN of *Atg7*$^{flox/flox}$;Pcp2-*Cre* mice at P56. *Atg7*$^{flox/flox}$ was used as control. (Scale bar: 10 μm.)

Atg7$^{flox/flox}$ mice did not exhibit significant difference in their cerebellar molecular layer thickness (Fig. 3 *A* and *B*). To evaluate changes in dendritic tree and spine morphology, we examined the expression pattern of metabotropic glutamate receptor 1α (mGluR1α) protein, a marker for parallel fiber–Purkinje cell synapses. No difference in localization and intensity of the anti-mGluR1α immunofluorescent staining was observed between the *Atg7*$^{flox/flox}$;Pcp2-*Cre* and *Atg7*$^{flox/flox}$ cerebellar molecular layers at either P35 (data not shown) or P56 (Fig. 3*C*). Thus, *Atg7* deletion had little effect on Purkinje cell dendritic tree and spine morphology up to at least P56. We conclude that *Atg7* deletion in Purkinje cells elicit differential effects on the dendritic and axonal compartments, suggesting that the axon terminals are particularly vulnerable to autophagy deficiency.

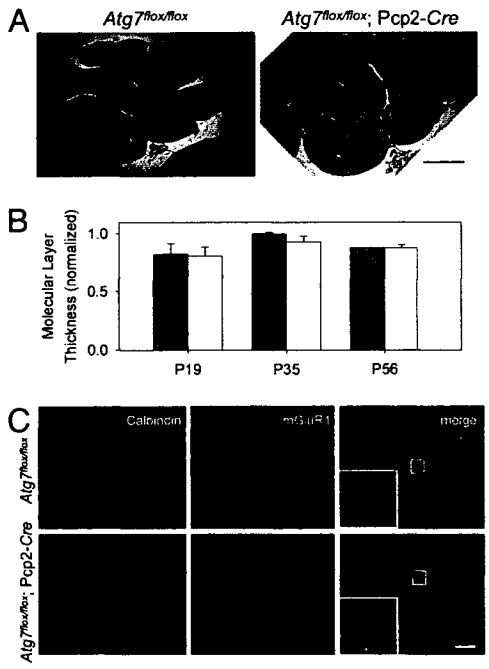

Fig. 3. Deletion of *Atg7* in Purkinje cells had little effect on the morphology of cerebellar cortex, Purkinje cell dendritic tree and spines in *Atg7*$^{flox/flox}$;Pcp2-*Cre* mice at P56. (*A*) H&E-stained images of midsagittal sections from *Atg7*$^{flox/flox}$ and *Atg7*$^{flox/flox}$;Pcp2-*Cre* cerebella at P56. (Scale bar: 0.5 mm.) n = 3–5. (*B*) Quantification of the molecular layer thickness (as the distance between lobules V and VI of the Purkinje cell layer divided by 2) from the cerebellar midsagittal sections of *Atg7*$^{flox/flox}$ and *Atg7*$^{flox/flox}$;Pcp2-*Cre* mice at P19, P35, and P56. n = 3–5. (*C*) Immunofluorescent staining of cerebellar midsagittal sections shows normal localization and appearance of mGluR1α (in red) in *Atg7*$^{flox/flox}$;Pcp2-*Cre* mice compared with *Atg7*$^{flox/flox}$ mice at P56. Green indicates anti-calbindin. (Scale bar: 10 μm.) n = 3.

Axonal Dystrophy Preceded Cell-Autonomous Degeneration of Purkinje Cells and Behavioral Deficits in *Atg7*$^{flox/flox}$;Pcp2-*Cre* Mice. To further evaluate the effects of *Atg7* deletion, we assayed for Purkinje cell degeneration and mouse behavioral deficits. Whereas the Purkinje cell axonal dystrophic swellings in the DCN of *Atg7*$^{flox/flox}$;Pcp2-*Cre* mice first became apparent at P19 and grew severe at P35 (Fig. 2*A*), no significant difference in Purkinje cell numbers was observed between the *Atg7*$^{flox/flox}$;Pcp2-*Cre* and *Atg7*$^{flox/flox}$ mice at both ages (Fig. 4 *A* and *B*). However, at P56, the number of Purkinje cells in *Atg7*$^{flox/flox}$;Pcp2-*Cre* mice was reduced by 28.4% ($P < 0.0005$) compared with *Atg7*$^{flox/flox}$ mice (Fig. 4 *A* and *B*). Thus, loss of Purkinje cells in *Atg7*$^{flox/flox}$;Pcp2-*Cre* mice occurred between P35 and P56. In comparison, the onset of axonal dystrophy began as early as P19. In addition, levels of GluRδ2 (a Purkinje cell-specific glutamate receptor subtype) in *Atg7*$^{flox/flox}$;Pcp2-*Cre* cerebellar extract were not reduced until P56 (SI Fig. 11), further supporting that the onset of axon dystrophy was earlier than Purkinje cell degeneration in *Atg7*$^{flox/flox}$;Pcp2-*Cre* mice.

Next, we assessed the locomotive behaviors in *Atg7*$^{flox/flox}$;Pcp2-*Cre* mice by limb-clasping, rotarod, and gait analyses at different postnatal ages. At P19 and P35, *Atg7*$^{flox/flox}$;Pcp2-*Cre* mice appeared normal and did not show any difference in performance compared with their control *Atg7*$^{flox/flox}$ littermates (data not shown). At P56, *Atg7*$^{flox/flox}$;Pcp2-*Cre* and *Atg7*$^{flox/flox}$ mice performed equally well on the rotarod and gait analyses (Fig. 4 *C* and *D*). However, 5 of 13 *Atg7*$^{flox/flox}$;Pcp2-*Cre* mice (38.5%) displayed limb-clasping reflexes on tail suspension, in comparison with 0 of 10 of their control littermates ($P < 0.01$). Thus, at P56, despite the 28.4% loss of Purkinje cells (Fig. 4*B*), *Atg7*$^{flox/flox}$;Pcp2-*Cre* mice displayed only mild behavioral impairment. In contrast, at 1 year, these mice demonstrated severe behavioral disorders in locomotion and motor coordination when evaluated in all three behavioral tests (Fig. 4 *C* and *D*; data not shown).

We summarize the temporal relationship of the morphological alterations, differential pathology in different compartments of Purkinje cells, and behavioral changes in *Atg7*$^{flox/flox}$;Pcp2-*Cre* mice in SI Table 1. These results demonstrate that axonal dystrophic swelling is an early pathogenic event and is likely to be a direct result of impairment of local autophagy in axon terminals.

Aberrant Membrane Structures Accumulated in the Dystrophic Axon Terminals of *Atg7*$^{flox/flox}$;Pcp2-*Cre* Purkinje Cells. To further assess the effect of impairment of autophagy on axon terminals, we characterized the axonal dystrophic swellings of *Atg7*$^{flox/flox}$;Pcp2-

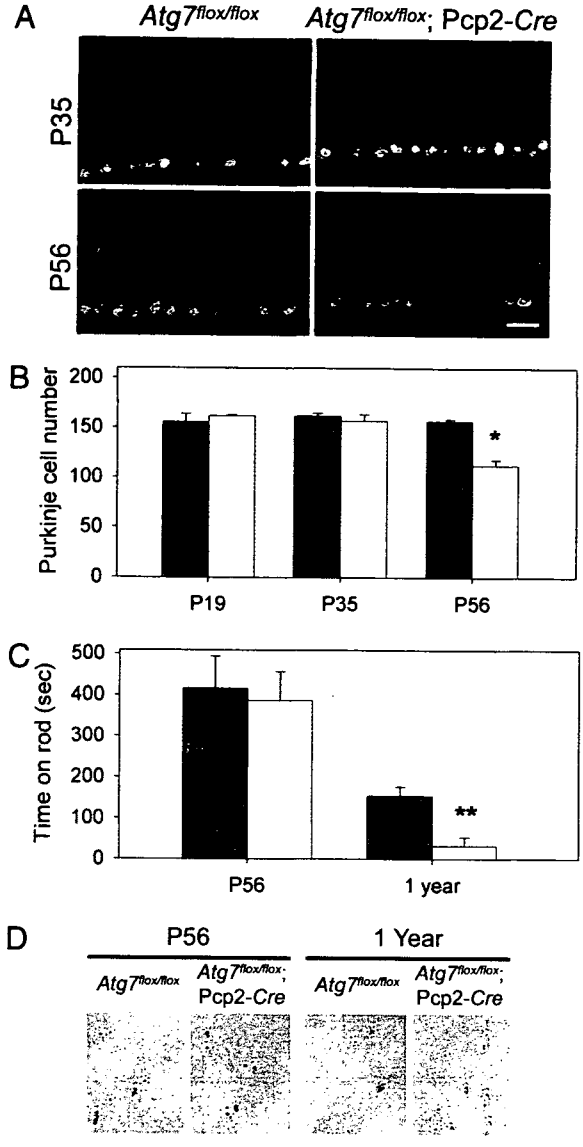

Fig. 4. Time course of Purkinje cell degeneration and locomotive behavioral deficits in *Atg7*$^{flox/flox}$;Pcp2-*Cre* mice. (*A*) Anti-calbindin immunofluorescent staining of the cerebellar midsagittal sections of *Atg7*$^{flox/flox}$ and *Atg7*$^{flox/flox}$;Pcp2-*Cre* mice at P35 and P56. (*B*) Quantitation of Purkinje cells at lobules IV–V of the midsagittal sections of *Atg7*$^{flox/flox}$ and *Atg7*$^{flox/flox}$;Pcp2-*Cre* mice at P19, P35, and P56 based on H&E-stained images. n = 3, 3, and 3 for *Atg7*$^{flox/flox}$ at P19, P35, and P56, respectively. n = 2, 3, and 5 for *Atg7*$^{flox/flox}$;Pcp2-*Cre* at P19, P35, and P56, respectively (*, $P < 0.0005$). (*C*) At P56, *Atg7*$^{flox/flox}$ and *Atg7*$^{flox/flox}$;Pcp2-*Cre* mice showed no significant difference in the time spent on the rod in rotarod assay. At 1 year, *Atg7*$^{flox/flox}$ mice spent much longer time on the rod than *Atg7*$^{flox/flox}$;Pcp2-*Cre* mice (**, $P < 0.05$). (*D*) In gait analyses at P56, *Atg7*$^{flox/flox}$ and *Atg7*$^{flox/flox}$;Pcp2-*Cre* mice showed similar step width and overlapping of forefeet and hindfeet (forefeet, red; hindfeet, black). At 1 year old, *Atg7*$^{flox/flox}$;Pcp2-*Cre* mice showed shorter step width than *Atg7*$^{flox/flox}$ mice as well as nonoverlapping forefeet and hindfeet (left feet, black; right feet, red). For both *C* and *D*, n = 5 at P56; n = 3 and 4 at 1 year.

Cre Purkinje cells by transmission electron microscopy. The cross-sections of the Purkinje cell axon terminals in the DCN of the *Atg7*$^{flox/flox}$ mice were normally 0.5–2 μm in diameter (Fig. 5*A*, white arrows). Remarkably, the swollen Purkinje cell axon terminals in the DCN of the *Atg7*$^{flox/flox}$;Pcp2-*Cre* mice often spanned 1–6 μm in diameter (Fig. 5 *B–F*, black arrows) and differed profoundly in their morphology from the axonal dystrophic swellings observed in *Lurcher* Purkinje cells (Fig. 5*G*, black arrows). The Purkinje cell axonal dystrophic swellings of *Lurcher* mice contained a large number of autophagosomes/autolysosomes (Fig. 5*G*), whereas those of the *Atg7*$^{flox/flox}$;Pcp2-*Cre* mice were devoid of autophagosomes (Fig. 2 and 6*Af*). However, these autophagasome-free swellings of the *Atg7*$^{flox/flox}$;Pcp2-*Cre* Purkinje cell axons often contained abnormal organelles or membrane structures (Fig. 5 *B–F*, white arrows), including stacks of cisternal membranes that formed lamellar bodies (Fig. 5 *B* and *E*, white arrows) (24), large and elaborate cisternal arrays and filaments (Fig. 5*F*, white arrow), and highly convoluted double-membrane whorls that occupied 1.5–2 μm of the swollen terminal (Fig. 5 *C* and *D*, white arrows). The exact nature of these aberrant structures was not clear; they were rarely seen in the somata of *Atg7*$^{flox/flox}$;Pcp2-*Cre* Purkinje cells (data not shown) or in the *Atg7*$^{flox/flox}$ Purkinje cells axons (Fig. 5*A*). However, it is noteworthy that the formation of convoluted membrane whorls was previously described in hepatocytes with *Atg7* deletion and was attributed to a failure in autophagic degradation (19). Our observations suggest a conserved function for autophagy in the clearance of cellular membranes and/or lipids in both axon terminals and hepatocytes.

Vacuole-Like Structures with Double Membranes Were Formed in Normal Purkinje Cell Axons but Were Absent in the Dystrophic Axon Terminals of *Atg7*$^{flox/flox}$;Pcp2-*Cre* Purkinje Cells. Interestingly, through further ultrastructural analysis, we observed vacuole-like structures with double membranes in the myelinated Purkinje cell axons in the DCN of control *Atg7*$^{flox/flox}$ mice (Fig. 6*Aa* and SI Fig. 12). These structures typically appeared to be closed and had diameters of 0.1–0.5 μm (Fig. 6*Aa*). We occasionally observed these double-membrane vacuole-like structures in the process of formation (Fig. 6*A b–e* and SI Fig. 12*A*). Many of these developing double-membrane vacuole-like structures appeared to be formed through invagination of the axolemma along the myelinated layers (Fig. 6*A b* and *c*, SI Fig. 12*A*), reminiscent of invasion by oligodendrocytic processes (25, 26). Some of them appear to be continuous with the axonal plasma membrane (Fig. 6*A d* and *e*), which are enwrapping portions of axoplasm (27). The average number of these distinct double-membrane vacuole-like structures (both closed and in the process of formation) in Purkinje cell axons of *Atg7*$^{flox/flox}$ mice was ≈0.9/50 μm^2 (Fig. 6*B*). In contrast, these structures were virtually absent in the *Atg7*$^{flox/flox}$;Pcp2-*Cre* mice (Fig. 6 *Af*, *B*, and *C*). Although we have yet to determine the exact nature of the vacuole-like structures with double membranes and their relationship with autophagosomes, our results suggested that *Atg7* was required for the formation of these distinct structures in axon terminals of normal Purkinje cells.

Discussion

Axonal dystrophic swelling is a hallmark of CNS axonopathy, which can be triggered by neuronal injuries, excitotoxicity, and various neurodegenerative conditions. Despite the prevalence of this pathology, the molecular mechanisms underlying axonopathy as well as the connection between axonopathy and neurodegeneration remain poorly understood (28). A critical question is whether axonal dystrophy and degeneration precede neuronal cell death or are secondary to neurodegeneration. Here, we analyzed the time course of pathological events after the deletion of the autophagy gene *Atg7* in cerebellar Purkinje cells. We showed that axonal dystrophy and degeneration caused by ablation of *Atg7* occurred much earlier than the onset of neuronal death, indicating that axonal dystrophy was not secondary to neurodegeneration. In addition, axonal dystrophy and degeneration was a cell-autonomous event, which precluded the action of glia as the primary cause of the axonal dystrophy in *Atg7*$^{flox/flox}$;Pcp2-*Cre* mice. Although this study was limited to Purkinje cells for the purpose of cell type-specific study of autophagy, axonal dystrophies occurred widely in many

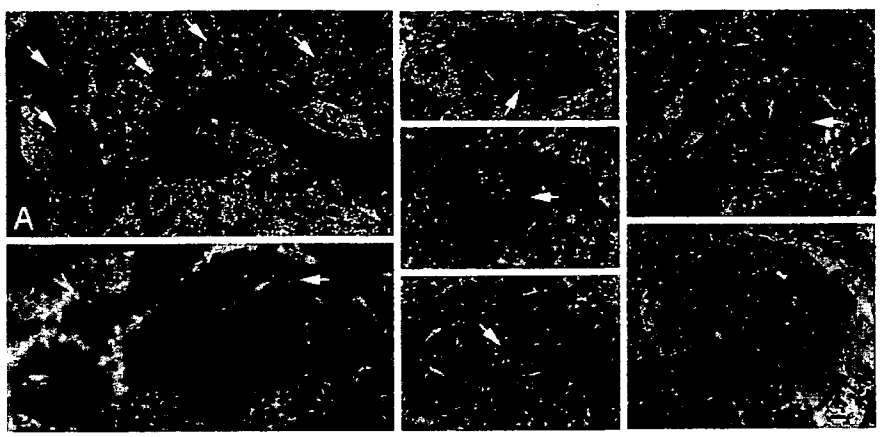

Fig. 5. Deletion of *Atg7* in Purkinje cells led to aberrant membrane structures in the axonal dystrophic swellings. Ultrastructural image of normal myelinated Purkinje cell axons (white arrows) and axon terminals (black arrows) in the DCN of $Atg7^{flox/flox}$ mice (*A*) and Purkinje cell axonal dystrophic swellings (black arrows) in the DCN of $Atg7^{flox/flox}$;Pcp2-*Cre* mice (*B–F*). (*B* and *E*) Stacks of cisternal membranes (white arrows). (*C* and *D*) Convoluted double-membrane whorls (white arrows). (*F*) The arrays of abnormal filaments (white arrows). (*G*) A dystrophic axon (black arrows) of *Lurcher* Purkinje cells containing numerous autophagosomes. (Scale bars: 500 nm.)

regions of the mutant mouse brain with *Atg7* or *Atg5* deletion (16, 17). We speculate that the axonal dystrophy associated with various types of neurons in these mutant mice are also cell-autonomous events caused by the absence of neuronal autophagy. Importantly, our results implied that interference in local autophagy would have a deleterious effect on axons, a potential mechanism of axonopathies involving impaired autophagy. Furthermore, we showed that deletion of *Atg7* had little effect on the overall morphology of the Purkinje cell dendritic arbors at a stage when axon terminals displayed massive dystrophy and degeneration. These differential effects of *Atg7* deletion suggested that basal levels of autophagy played a particularly important role in housekeeping functions in axon terminals and in protection against axonal degeneration.

We showed that *Atg7* was indispensable for the formation of the distinctive vacuole-like structures with double membranes, which were normally present within wild-type Purkinje cell axons. These structures have not been described previously in the wild-type Purkinje cell axons. Although the majority of these structures were likely derived from invagination of neighboring oligodendrocytes (Fig. 6*A b* and *c* and SI Fig. 12*A*) (25, 26), some of them appeared to originate from axonal subsurface cisternae (27) or smooth endoplasmic reticulum (29) (Fig. 6*A d* and *e*). Although we have yet to determine the nature of these structures, we cannot exclude the possibility that some of these structures are autophagosome-related vacuoles. A previous study has shown the presence and transport of autophagosomes in the axons of cultured sympathetic neurons, despite that the physiological function of autophagy in the axons is unknown (30). Regardless of the nature of these vacuole-like structures, *Atg7* deletion abolished their formation, and caused axonal swelling and accumulation of aberrant membrane structures in these swellings. These results established an important role of *Atg7* in regulating local membrane trafficking and turnover. However, an important question arising from these results is whether the requirement of *Atg7* for the formation of the double-membrane vacuole-like structures is somehow connected to autophagy or associated with a specific Atg7 function independent of autophagy. Current evidence suggests that *Atg7* function is exclusively associated with autophagy. Consistent with this idea, the abolishment of the double-membrane vacuole-like structures caused by *Atg7* deletion can be explained by the failure of autophagy, which would

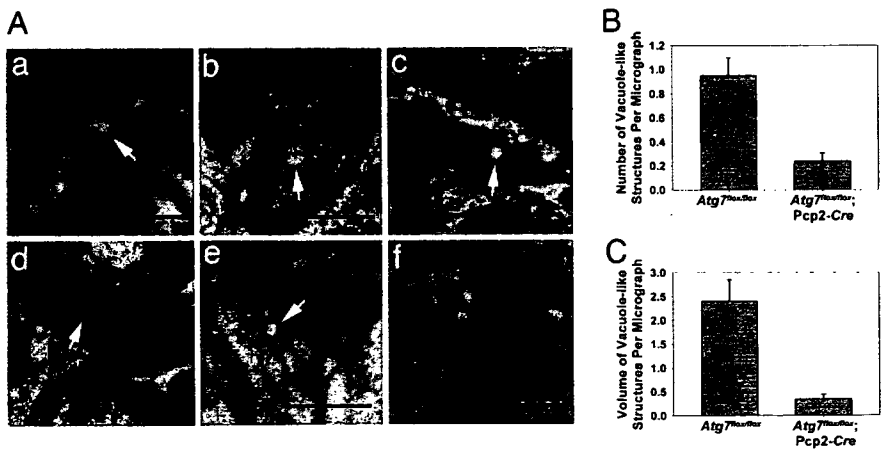

Fig. 6. Deletion of *Atg7* in Purkinje cells abolished double-membrane vacuole-like structures in their axon terminals in the DCN. (*A*) Ultrastructural images show the presence of vacuole-like structures with double membranes in Purkinje cell preterminal axons of $Atg7^{flox/flox}$ mice (*a–e*, white arrows) and the abolishment of these structures in $Atg7^{flox/flox}$;Pcp2-*Cre* mice (*f*) at P35. (Scale bars: 0.5 μm.) (*B*) Comparison of the numbers of these vacuole-like structures per transmission electron microscopy micrograph (50 μm^2) in the DCN of $Atg7^{flox/flox}$;Pcp2-*Cre* versus $Atg7^{flox/flox}$ mice (ratio, 4.0; $P = 0.00003$). (*C*) Comparison of the volume fraction of double-membrane vacuole-like structures by point counting of transmission electron microscopy micrographs in the DCN of $Atg7^{flox/flox}$;Pcp2-*Cre* versus $Atg7^{flox/flox}$ mice (ratio, 6.9; $P = 0.00002$).

normally participate in the formation of these structures. Thus, we hypothesize that, in addition to the role in protein quality control (16, 17), neuronal autophagy regulates membrane homeostasis in the axon terminals. Furthermore, we showed that deletion of *Atg7* caused the axonal terminal swelling, which was a reminiscence of hepatic cell swelling in *Atg7*-deleleted mouse liver (19). It is conceivable that axon terminals and hepatocytes may share a similar mechanism for cell (or cellular compartment) size control, which requires autophagy (31).

Previous morphological studies have consistently shown the presence of large numbers of autophagosome-like vacuoles in axonal dystrophic swellings of injured neurons (4–13). We have previously demonstrated that induction of autophagy in *Lurcher* Purkinje cells involved accumulation of autophagosomes in the dystrophic axons (22). In contrast, our present study shows that the axonal swellings of Purkinje cells in $Atg7^{flox/flox}$;Pcp2-*Cre* mice were devoid of vacuoles that resembled the autophagosomes observed in *Lurcher* mice. Although our present study demonstrates a role for basal levels of autophagy in axonal protection and indicates that altered autophagy could serve as an adaptive response for remodeling the axon terminals for regeneration (3, 22), we cannot exclude the possibility that up-regulation of autophagy in dystrophic axons is actually destructive, causing overdegradation of axonal structures. This possibility can be tested, in principle, by genetic crossing of the autophagy-deficient mice with diseased mice containing the autophagosome-like vacuoles in dystrophic axons or cell bodies.

In summary, our study provides genetic and molecular evidence for the indispensable role of neuronal autophagy in the maintenance of axonal homeostasis, particularly in local membrane trafficking and turnover. Perturbation of local autophagy in the axons leads to axonopathy. We believe that it is important to study the connection between axonal autophagy impairment and human neuropathological conditions associated with axonal dystrophy.

Materials and Methods

Antibodies. Antibodies used were mouse monoclonal anti-calbindin D-28K (Swant, Bellinzona, Switzerland), anti-calbindin (Sigma, St. Louis, MO), anti-GluRδ2 (BD Transduction Laboratories, San Diego, CA), anti-p62 (American Research Products, Belmont, MA), Cy3-conjugated anti-mouse and anti-rabbit IgG (Upstate Biotechnology, Lake Placid, NY), and NeuN, mGluR1α, and actin antibodies (Chemicon International, Temecula, CA). Anti-Atg7 is described in ref. 19.

Animals. Pcp2-Cre transgenic mice (20) (The Jackson Laboratory, Bar Harbor, ME) and $Atg7^{flox/flox}$ mice (19) were crossed to produce $Atg7^{flox/flox}$;Pcp2-*Cre* mice. $Atg7^{flox/flox}$;Pcp2-*Cre* mice and GFP-LC3 transgenic mice (2) were crossed to produce $Atg7^{flox/flox}$;Pcp2-*Cre*/GFP-LC3 mice.

Histological Examination. Mice were fixed by cardiac perfusion with 0.1 M phosphate buffer containing 4% paraformaldehyde. The color images of the Meyer's H&E-stained midsagittal cryosections (10 μm) of cerebella were acquired with a 20× objective lens and a color CCD camera, and later assembled to full images in Photoshop for the quantification of Purkinje cells. Immunofluorescent stained cerebellar samples were prepared as described in ref. 22 and examined by using confocal microscopy.

Behavioral Analyses. Motor function was assessed by the limb-clasping test, rotarod assay, and gait analysis (*SI Materials and Methods*).

Electron Microscopy. Tissue samples were obtained from three $Atg7^{flox/flox}$ mice and three $Atg7^{flox/flox}$;Pcp2-*Cre* mice. Details of the experiment are described in *SI Materials and Methods*. In brief, thin sections (70 nm) of the lateral cerebellar nucleus and cerebellar cortex were prepared and examined by transmission electron microscopy (H7500; Hitachi, Tokyo, Japan). A double-blind point-counting method was used to quantify double-membrane vacuole-like structures in 55 micrographs of either $Atg7^{flox/flox}$ or $Atg7^{flox/flox}$;Pcp2-*Cre* mice. The total number of these structures overlying at least one intersection of a Photoshop-generated grid was counted to be 52 and 13 for $Atg7^{flox/flox}$ and $Atg7^{flox/flox}$;Pcp2-*Cre* samples, respectively. The total number of intersections within these structures was 132 and 19 for $Atg7^{flox/flox}$ and $Atg7^{flox/flox}$;Pcp2-*Cre* samples, respectively.

Statistical Analyses. The equality of the variance was first tested by using the F test. Pair-wise comparisons were calculated by using one-tailed Student's t test. The standard error was calculated for each sample.

We thank X. Li, Y. Ding, T. Kouno, and K. Tatsumi for excellent technical assistance; A. North in the Rockefeller Bio-Imaging Resource Center for help with microscopy; and S. Waguri, T. Ueno, I. Tanida, J. Ezaki, and N. Heintz for helpful discussion. This study was supported by National Institutes of Health Grants RNS055683A (to Z.Y.), RR00862, and RR022220 (both to B.T.C.).

1. Levine B, Klionsky DJ (2004) *Dev Cell* 6:463–477.
2. Mizushima N, Yamamoto A, Matsui M, Yoshimori T, Ohsumi Y (2004) *Mol Biol Cell* 15:1101–1111.
3. Rubinszstein DC, DiFiglia M, Heintz N, Nixon RA, Qin ZH, Ravikumar B, Stefanis L, Tolkovsky A (2005) *Autophagy* 1:11–22.
4. Yue Z, Horton A, Bravin M, DeJager PL, Selimi F, Heintz N (2002) *Neuron* 35:921–933.
5. Dixon JS (1967) *Nature* 215:657–658.
6. Matthews MR, Raisman G (1972) *Proc R Soc Lond Ser B* 181:43–79.
7. Nixon RA, Wegiel J, Kumar A, Yu WH, Peterhoff C, Cataldo A, Cuervo AM (2005) *J Neuropathol Exp Neurol* 64:113–122.
8. Cataldo AM, Hamilton DJ, Barnett JL, Paskevich PA, Nixon RA (1996) *J Neurosci* 16:186–199.
9. Anglade P, Vyas S, Javoy-Agid F, Herrero MT, Michel PP, Marquez J, Mouatt-Prigent A, Ruberg M, Hirsch EC, Agid Y (1997) *Histol Histopathol* 12:25–31.
10. Roizin L, Stellar S, Willson N, Whittier J, Liu JC (1974) *Trans Am Neurol Assoc* 99:240–243.
11. Sikorska B, Liberski PP, Giraud P, Kopp N, Brown P (2004) *Int J Biochem Cell Biol* 36:2563–2573.
12. Yu WH, Cuervo AM, Kumar A, Peternoff CM, Schmidt SD, Lee JH, Mohan PS, Mercken M, Farmery MR, Tjernberg LO, *et al.* (2005) *J Cell Biol* 171:87–98.
13. Lin WL, Lewis J, Yen SH, Hutton M, Dickson DW (2003) *J Neurocytol* 32:1091–1105.
14. Li H, Li SH, Yu ZX, Shelbourne P, Li XJ (2001) *J Neurosci* 21:8473–8481.
15. Coleman MP, Perry VH (2002) *Trends Neurosci* 25:532–537.
16. Komatsu M, Waguri S, Chiba T, Murata S, Iwata J, Tanida I, Ueno T, Koike M, Uchiyama Y, Kominami E, *et al.* (2006) *Nature* 441:880–884.
17. Hara T, Nakamura K, Matsui M, Yamamoto A, Nakahara Y, Suzuki-Migishima R, Yokoyama M, Mishima K, Saito I, Okano H, *et al.* (2006) *Nature* 441:885–889.
18. Ohsumi Y, Mizushima N (2004) *Semin Cell Dev Biol* 15:231–236.
19. Komatsu M, Waguri S, Ueno T, Iwata J, Murata S, Tanida I, Ezaki J, Mizushima N, Ohsumi Y, Uchiyama Y, *et al.* (2005) *J Cell Biol* 169:425–434.
20. Barski JJ, Dethleffsen K, Meyer M (2000) *Genesis* 28:93–98.
21. Kabeya Y, Mizushima N, Ueno T, Yamamoto A, Kirisako T, Noda T, Kominami E, Ohsumi Y, Yoshimori T (2000) *EMBO J* 19:5720–5728.
22. Wang QJ, Ding Y, Kohtz S, Mizushima N, Cristea IM, Rout MP, Chait BT, Zhong Y, Heintz N, Yue Z (2006) *J Neurosci* 26:8057–8068.
23. Bjorkoy G, Lamark T, Brech A, Outzen H, Perander M, Overvatn A, Stenmark H, Johansen T (2005) *J Cell Biol* 171:603–614.
24. Banno T, Kohno K (1998) *J Comp Neurol* 402:252–263.
25. Zhang P, Land W, Lee S, Juliani J, Lefman J, Smith SR, Germain D, Kessel M, Leapman R, Rouault TA, *et al.* (2005) *J Struct Biol* 150:144–153.
26. Eddleman CS, Ballinger ML, Smyers ME, Fishman HM, Bittner GD (1998) *J Neurosci* 18:4029–4041.
27. Li YC, Li YN, Cheng CX, Sakamoto H, Kawate T, Shimada O, Atsumi S (2005) *Neurosci Res* 53:298–303.
28. Coleman M (2005) *Nat Rev Neurosci* 6:889–898.
29. Broadwell RD, Cataldo AM (1984) *J Comp Neurol* 230:231–248.
30. Hollenbeck PJ (1993) *J Cell Biol* 121:305–315.
31. Hosokawa N, Hara Y, Mizushima N (2006) *FEBS Lett* 580:2623–2629.

MOLECULAR AND CELLULAR BIOLOGY, Oct. 2007, p. 6629–6638 Vol. 27, No. 19
0270-7306/07/$08.00+0 doi:10.1128/MCB.00509-07

Rpn10-Mediated Degradation of Ubiquitinated Proteins Is Essential for Mouse Development[▽]

Jun Hamazaki,[1,2] Katsuhiro Sasaki,[1] Hiroyuki Kawahara,[3] Shin-ichi Hisanaga,[2] Keiji Tanaka,[1] and Shigeo Murata[1]*

Laboratory of Frontier Science, Core Technology and Research Center, Tokyo Metropolitan Institute of Medical Science, Bunkyko-ku, Tokyo 113-8613,[1] Department of Biological Sciences, Graduate School of Science, Tokyo Metropolitan University, Hachiohji, Tokyo 192-0397,[2] and Department of Biochemistry, Graduate School of Pharmaceutical Science, Hokkaido University, Sapporo 060-0812,[3] Japan

Received 23 March 2007/Returned for modification 21 May 2007/Accepted 16 July 2007

Rpn10 is a subunit of the 26S proteasome that recognizes polyubiquitinated proteins. The importance of Rpn10 in ubiquitin-mediated proteolysis is debatable, since a deficiency of Rpn10 causes different phenotypes in different organisms. To date, the role of mammalian Rpn10 has not been examined genetically. Moreover, vertebrates have five splice variants of Rpn10 whose expressions are developmentally regulated, but their biological significance is not understood. To address these issues, we generated three kinds of Rpn10 mutant mice. Rpn10 knockout resulted in early-embryonic lethality, demonstrating the essential role of Rpn10 in mouse development. Rpn10a knock-in mice, which exclusively expressed the constitutive type of Rpn10 and did not express vertebrate-specific variants, grew normally, indicating that Rpn10 diversity is not essential for conventional development. Mice expressing the N-terminal portion of Rpn10, which contained a von Willebrand factor A (VWA) domain but lacked ubiquitin-interacting motifs (Rpn10ΔUIM), also exhibited embryonic lethality, suggesting the important contribution of UIM domains to viability, but survived longer than Rpn10-null mice, consistent with a "facilitator" function of the VWA domain. Biochemical analysis of the Rpn10ΔUIM liver showed specific impairment of degradation of ubiquitinated proteins. Our results demonstrate that Rpn10-mediated degradation of ubiquitinated proteins, catalyzed by UIMs, is indispensable for mammalian life.

The ubiquitin-proteasome system is the main nonlysosomal apparatus for intracellular protein degradation that is conserved in all eukaryotes from *Saccharomyces cerevisiae* to mammals (10, 15). Short-lived proteins as well as abnormal proteins are mostly recognized by the ubiquitin system and are tagged with ubiquitin chains as degradation signals. The polyubiquitinated proteins are then targeted for degradation by 26S proteasomes.

The 26S proteasome is composed of one proteolytically active 20S proteasome (also called the core particle) and two 19S regulatory particles (RP), each attached to one end of the 20S proteasome (1). The 19S RP plays an essential role in the degradation of ubiquitinated proteins. The 19S RP can be divided into two subcomplexes, known as the "base" and the "lid" (11). Structurally, the base subcomplex is made up of six different ATPases (Rpt1 to Rpt6) and two large subunits called Rpn1 and Rpn2, which act as scaffolds for molecules that modulate proteasome functions, such as Rpn13, Ubp6 (an USP14 orthologue), and Rad23 (an mHR23A/B orthologue) (4, 5, 13, 17, 24, 29, 35, 50). The base binds to the α-ring of the 20S proteasome and opens its narrow gate in an ATP-dependent manner (39). In addition, the ATPase subunits supply energy for unfolding target proteins, so that they can be translocated into the interior cavities of 20S proteasomes, where the active sites are located. The lid subcomplex consists of multiple non-ATPase subunits (Rpn3, Rpn5 to -9, Rpn11, Rpn12, and Rpn15). The role of the lid complex is less well understood, but it is reported to be essential for the degradation of ubiquitinated proteins, at least through the function of Rpn11, which deubiquitinates ubiquitin chains of proteasome substrates prior to degradation (44, 49).

In the ubiquitin-proteasome pathway, the process through which the polyubiquitin chains are recognized by the proteasome remains elusive. To date, several proteins have been identified as receptors that bind ubiquitinated proteins to ferry them to proteasomes for degradation. The UBL-UBA proteins, which contain ubiquitin-like (UBL) and ubiquitin-associated (UBA) domains, can interact with the proteasome through their N-terminal UBL domains as well as with polyubiquitin chains through their C-terminal UBA domains and are thought to shuttle ubiquitinated substrates to the proteasome and to facilitate their degradation (2, 8, 34). There are three UBL-UBA proteins in budding yeast called Rad23, Ddi1, and Dsk2 (2, 8, 34). Furthermore, several UBL-UBA proteins are also found in mammals, and some of them act in a manner similar to that of their yeast counterparts (12, 21).

Polyubiquitinated proteins are also recognized directly by the 19S proteasome subunit Rpn10 (3). Rpn10 is composed of one N-terminal von Willebrand factor A (VWA) domain and one or two C-terminal ubiquitin-interacting motifs (UIM). Rpn10 was the first protein recognized to bind to polyubiquitin chains through UIM domains. Surprisingly, genetic studies

* Corresponding author. Mailing address: Laboratory of Frontier Science, Core Technology and Research Center, Tokyo Metropolitan Institute of Medical Science, Bunkyko-ku, Tokyo 113-8613, Japan. Phone and fax: 81-3-3823-2237. E-mail: smurata@rinshoken.or.jp.

▽ Published ahead of print on 23 July 2007.

TABLE 1. Genotyping PCR primers[a]

Primer name	Sequence (5′–3′)
a	CAAGTAGTGCCTCTGGCTGCAAGA
b	TCCTGTCATCTCACCTTGCTCCTG
c	CTTGGGAGGCAGAGACAGATGGAT
d	AGGGACAAGAACAGCCCATGTCTGATTC
e	GATGCAATGCGGCGGCTGCATACGCTTG
f	ATGGCCGCTCACAACTGTCTGCAACTCC
g	CCTGTGTAGGATACCACAGCATCGACT
h	ATTGCTGGGAGTATGAACCACCATGCTG

[a] Primers a, b, and c were used for genotyping of Rpn10 knockout mice. Primers d, e, and f were used for Rpn10a knock-in mouse genotyping. Primers f, g, and h were used for Rpn10ΔUIM mouse genotyping.

TABLE 2. PCR primers for Rpn10 splicing variants

Primer name	Sequence (5′–3′)
Rpn10a,c,d,e forward	CAAAGGCAAGATCACCTTCTGCACTGGCA
Rpn10b forward	TACACCTGGGACTGAAGGTGAAAGA
Rpn10a,b reverse	GTTCTCTAGGACGCTCTG
Rpn10c reverse	AAGTGTTTCCTTCTGTTGCTCCAAG
Rpn10d reverse	GGCCCTGCCACCCAAGCCATGGCCCAC
Rpn10e reverse	TCGTGAAATGGCTAGCAC

with yeast showed that deletion of the gene resulted in little loss of viability, in contrast to most other proteasome genes, which are essential for life (6, 43). The degradation defect of the *rpn10Δ* strain is modest, and the defect becomes evident when the strain is crossed with strains that lack UBL-UBA proteins such as Rad23 and Dsk2 (23, 31). In vitro analysis of the degradation of polyubiquitinated Sic1 showed that while its degradation was defective in *rpn10Δ* proteasomes and *rad23Δ* proteasomes, simultaneous addition of Rad23 protein and the VWA domain of Rpn10 restored the degradation of ubiquitinated Sic1, suggesting a "facilitator" activity within the VWA domain of Rpn10 (45). Finally, a yeast strain that has mutations in the UIM domain of Rpn10 showed a clear deficiency in ubiquitin chain recognition, and this *rpn10-uim* mutation confers synthetic sensitivity to canavanine when combined with either a *rad23Δ* or a *dsk2Δ* mutation, indicating that the UIM domain of Rpn10 and UBL-UBA proteins work redundantly (4). It is now suggested that UBL-UBA proteins and Rpn10 define a layer of substrate selectivity, which might depend on the length of polyubiquitin chains (6, 20, 30, 45).

Although Rpn10 is not essential for life or for overall ubiquitin-mediated protein turnover in yeast and worm (6, 36, 41, 43), Rpn10-deficient mutants of *Physcomitrella patens*, *Arabidopsis thaliana*, and *Drosophila melanogaster* showed more-severe phenotypes such as developmental arrest and lethality (9, 38, 40). These results suggest that higher eukaryotes depend on Rpn10-mediated degradation of polyubiquitinated proteins for their development.

Vertebrates have acquired a diversity of proteasomes by creating new subunits. For example, the gamma interferon-inducible subunits β1i, β2i, and β5i evolved to produce immunoproteasomes, which enable viral proteins to be presented on major histocompatibility complex class I molecules more efficiently than constitutive proteasomes (42). Vertebrates have also acquired a diversified Rpn10 subunit, which was accomplished by developmentally regulated alternative splicing, resulting in the generation of five isoforms named Rpn10a to Rpn10e (see Fig. 1A) (18). It is reported that Rpn10c in *Xenopus laevis* associates with Scythe/BAG-6 and regulates apoptosis (19). However, the significance and distinct functions of these isoforms in mammals are not understood at all. In addition, the importance of the UIM and VWA domains of Rpn10 for mammalian development has not been examined.

In the present study, we generated and analyzed three types of Rpn10 mutant mice in order to understand the role(s) of Rpn10 in mammals. Our results provide genetic evidence for the in vivo significance of Rpn10 in mammals.

MATERIALS AND METHODS

Gene targeting of Rpn10. A targeting vector for Rpn10-null mice was constructed by replacing exons 2 to 8 with a neomycin resistance gene (*neo*) cassette. For Rpn10a knock-in mice (with, at the same time, conditional deletion of UIM domains), exons 7 to 10 were replaced with the corresponding cDNA of Rpn10a, with a polyadenylation signal attached at its 3′ end. A *neo* cassette was inserted at the 3′ end of the cDNA. LoxP sequences were inserted at the 5′ end of the cDNA and the 3′ end of the *neo* cassette. TT2 embryonic stem cells were screened as described previously (27). For Southern blot analysis, genomic DNA was digested with EcoRI for Rpn10 knockout or with EcoRV for Rpn10a knock-in and was hybridized with the probes shown in Fig. 1A and 2A, respectively. EIIa-Cre and Alb-Cre were purchased from The Jackson Laboratory. PCR primers used for mouse genotyping are listed in Table 1. Mice were housed in pathogen-free facilities, and the experimental protocol was approved by the Ethics Review Committee for Animal Experimentation of the Tokyo Metropolitan Institute of Medical Science.

RNA isolation, reverse transcription, and real-time PCR. Expression levels of Rpn10 variants were determined by reverse transcription-PCR (RT-PCR) as described previously (18). Specific primers for each variant are listed in Table 2. For real-time PCR analysis, total RNAs were isolated from the livers of 5-week-old mice by using an RNAspin minikit (GE Healthcare), reverse transcribed to cDNA using a Transcriptor first-strand cDNA synthesis kit (Roche), and subjected to real-time PCR using the LightCycler 480 system (Roche). PCR primers and universal probes (Roche), which are listed in Table 3, were designed according to the Universal Probe Assay Design Center (http://www.roche-applied-science.com/sis/rtpcr/upl/adc.jsp). Glucuronidase beta (GUSβ) was used for normalization. Real-time PCR data were analyzed by the $\Delta\Delta C_T$ method.

Immunological analysis. Mouse livers were homogenized and subjected to immunoblotting and immunoprecipitation as described previously (13). The antibodies against Rpn1, Rpn3, Rpt6, the VWA domain of Rpn10 [Rpn10(N)], USP14, polyubiquitin, and actin have been described previously (13). Polyclonal antibodies against a6, a7, Rpn6, Rpn7, Rpt3, Rpt5, the UIM domain of Rpn10 [Rpn10(C)], and mHR23B (all sequences were derived from mice) were raised in rabbits by using recombinant proteins expressed in and purified from strain BL21RIL (Novagen) as His_6 fusion proteins of α6 (residues 152 to 263), α7 (residues 157 to 255), Rpn6 (residues 1 to 162), Rpn7 (residues 1 to 137), Rpt3 (residues 1 to 100), and Rpt5 (residues 1 to 131) and as glutathione *S*-transferase fusion proteins of Rpn10 (residues 255 to 376) and mHR23B (full length), respectively. For immunoprecipitation, a liver homogenate from an $Rpn10^{a/a}$ or an $Rpn10^{a/a:Alb}$ mouse (the two mice had equal Suc-LLVY hydrolyzing activities) was immunoprecipitated with an anti-Rpt6 antibody.

Glycerol gradient analysis. Mouse liver homogenates were clarified by centrifugation at 20,000 × *g* and subjected to 10 to 40% (vol/vol) linear glycerol gradient centrifugation (22 h, 83,000 × *g*) as described previously (16).

Assay of proteasome activity. The assays of proteasome chymotryptic peptidase activity, degradation of recombinant ^{35}S-labeled ornithine decarboxylase (ODC), and degradation of polyubiquitinated ^{35}S-labeled cIAP1 protein have been described previously (13, 16).

Histological examination. Embryos in utero were fixed in 4% paraformaldehyde, embedded in paraffin, and sectioned. Sections were stained with Mayer's hematoxylin, followed by eosin staining.

Culture of blastocysts. Blastocysts were flushed out from pregnant female uteri at embryonic day 3.5 (E3.5) and were cultured in M16 medium (Sigma-Aldrich) at 37°C under 5% CO_2 on a gelatin-coated chambered coverglass (Nalgene).

TABLE 3. PCR primers and universal probes for real-time PCR

Gene	Probe no.	Forward primer (5′-3′)	Reverse primer (5′-3′)
GUS	6	GATGTGGTCTGTGGCCAAT	TGTGGGTGATCAGCGTCTT
α5	25	TCGCTCATCATCCTCAAGC	AAATTCTGACCAGGCTGCAC
α6	80	CCGTTCTCAATCAGCTCGTA	ACCAGTTCATCCAAATTGCAC
Rpn3	32	TCCACAACATGTCTGTCAAGG	CCTTGGCAAACTCCAGGTC
Rpn7	29	TAGGTCATTAACCCTCGGCTAT	CTTCCAGCAGCAATAAACCTG
Rpt3	22	GTCGCCAGAAGAGGTTGATT	ATCTGGACGGGCCACATA
Rpt5	74	GGGTTGGACATGCTTGGT	CCTGGGCAACGTGTTTCT
mHR23B	2	CTGGAAGTGGGCACATGAAT	TTCAGGAAATCCTAATGCCTTT
USP14	18	GGCGAACAAGGGCAGTATC	TCTGTTGCAGGACTCTCATCA

RESULTS

Loss of Rpn10 causes early embryonic lethality in mice. To determine the significance of Rpn10 in mammals, we generated Rpn10-null mice by replacing exons 2 to 8 with a neomycin resistance gene (Fig. 1B to D). Rpn10-heterozygous ($Rpn10^{+/-}$) mice were born without any gross abnormality and were fertile. These mice were intercrossed to produce $Rpn10^{-/-}$ mice. The progeny did not contain surviving $Rpn10^{-/-}$ pups, suggesting that the absence of Rpn10 during embryogenesis is lethal. To investigate this issue further, we examined, at various stages of development (mainly E6.5 to E7.5), embryos that had been produced in timed intercrosses. In normal E6.5 embryos, a cylinder-like two-layered cellular structure was observed. However, Rpn10-deficient embryos failed to form this structure at E6.5 (Fig. 1E, left) and were resorbed by E7.5 (Fig. 1E, right).

To analyze further the defects associated with Rpn10 deficiency, we isolated blastocysts from $Rpn10^{+/-}$ intercrosses at E3.5. $Rpn10^{-/-}$ blastocysts were identified by PCR at the expected Mendelian frequency (Fig. 1F, left; also data not shown), representing relatively mild phenotypes compared to those of Rpt3 and Rpt5 knockout mice, which did not develop beyond the 8-cell stage (33). When these blastocysts were cultured in vitro, most of the $Rpn10^{-/-}$ blastocysts hatched from the zona pellucida, spread trophoblastic cells with proliferating inner cell masses (ICMs), which form the future embryonic ectoderm, and grew on the gelatin-coated glass, like wild-type blastocysts (Fig. 1F, center). However, ICMs of $Rpn10^{-/-}$ blastocysts could not expand beyond 48 h of culture and detached from the trophoblastic cells before 96 h of culture, in contrast to wild-type ICMs (Fig. 1F, right). These results indicate that Rpn10 is essential for embryonic development beyond blastocyst formation; presumably it is involved in the expansion of the embryonic ectoderm after implantation.

Rpn10a is sufficient for the development of mice. In vertebrates, Rpn10 has five splice variants named Rpn10a to Rpn10e. Rpn10a is the conventional isoform expressed throughout development and throughout the body, while Rpn10b to Rpn10e are expressed at specific developmental stages or in specific organs (Fig. 1A). These facts raise the possibility that the diversity of Rpn10 plays a role in development in vertebrates. To test this hypothesis and to clarify the roles of these vertebrate-specific isoforms, we generated Rpn10a knock-in mice. The Rpn10 isoforms are generated by different splice acceptor and donor usages of a genomic locus that corresponds to exons 7 to 10 of the Rpn10a isoform, which encode the major part of the two UIM domains of Rpn10 (18). Therefore, a targeting vector was designed to replace a genomic locus with the corresponding cDNA sequences of Rpn10a and to disrupt the expression of other isoforms (Fig. 2A to C). The inserted Rpn10a cDNA was flanked with *loxP* sequences to enable the generation of mice expressing Rpn10 lacking UIM domains (Rpn10ΔUIM). Mice heterozygous for the Rpn10a knock-in allele ($Rpn10^{a/+}$ mice) were born healthy and fertile without noticeable pathological phenotypes. $Rpn10^{a/a}$ mice, obtained by intercrossing $Rpn10^{a/+}$ mice, were born healthy at Mendelian frequency, were fertile, and grew apparently normally without any gross abnormality (data not shown). RT-PCR analysis of RNAs from newborn mice demonstrated loss of Rpn10b to Rpn10e isoforms in $Rpn10^{a/a}$ mice, while all the isoforms were expressed in wild-type mice (Fig. 2D). The protein levels of Rpn10 as well as other proteasome subunits in $Rpn10^{a/a}$ mice were similar to those in the wild type (Fig. 2E), and the expressed Rpn10a was incorporated normally into 26S proteasomes, like that expressed in wild-type mice (Fig. 2F, right). The proteasome activity of the $Rpn10^{a/a}$ liver, assessed with fluorogenic peptides, was nearly equal to that of the wild-type liver (Fig. 2F, right). The proteasome activities of adult brains were also comparable in $Rpn10^{a/a}$ and wild-type mice (data not shown). These results indicate that vertebrate-specific isoforms of Rpn10 do not play an important role in development and that the conventional isoform Rpn10a is sufficient for life, at least under normal circumstances. However, it is possible that isoforms Rpn10b to Rpn10e are involved in the degradation of specific target proteins or play a role in a process other than ubiquitin-mediated proteolysis, defects in which might become apparent only under certain conditions.

Mice deficient in UIM domains exhibit embryonic lethality but survive longer than Rpn10-null mice. In genetic analyses using yeast and moss, lack of the UIM domains of Rpn10 displayed modest phenotypes compared to null mutations, thus questioning the physiological significance of the UIM domains of Rpn10 (6, 9). To examine the role of these domains in mice, we generated Rpn10ΔUIM-expressing mice by Cre recombinase-mediated excision of the UIM domain-coding region (Fig. 2A, bottom, and Fig. 3A). By crossing $Rpn10^{a/a}$ mice with EIIa-Cre transgenic mice, in which the expression of Cre recombinase appears from the zygote stage (22), we obtained mice harboring an Rpn10 gene encoding Rpn10ΔUIM protein throughout the body, including germ cells ($Rpn10^{\Delta UIM/+}$ mice). $Rpn10^{\Delta UIM/+}$ mice were born at the expected Mende-

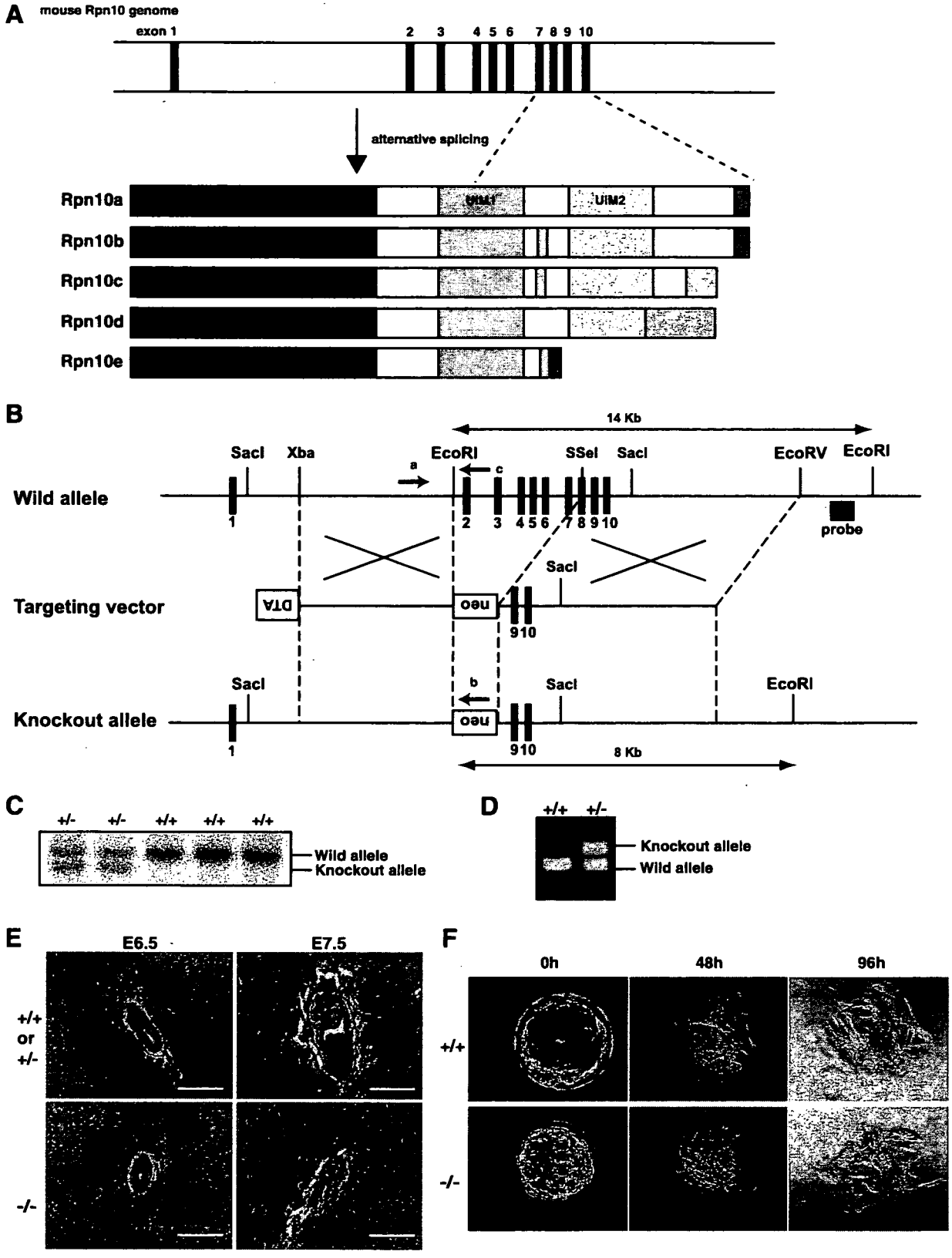

FIG. 1. Death in utero of Rpn10-deficient mouse embryos at E6.5. (A) Schematic representation of the Rpn10 gene and a family of mouse Rpn10 proteins. (Top) Physical map of the Rpn10 gene. Exons are indicated by filled rectangles and are numbered from 1 to 10 (upper panel). (Bottom) The structures of multiple Rpn10 proteins (Rpn10a to Rpn10e) generated by alternative splicing are shown schematically. Red, blue, and yellow represent the VWA, UIM1, and UIM2 domains, respectively. The sequences specific to each variant are represented by various colors. For details of the generation of the variants listed, see reference 18. (B) Schematic representation of the targeting vector and the targeted allele of the

lian frequency but exhibited slightly retarded growth and maturation compared to wild-type mice or even to $Rpn10^{+/-}$ mice (data not shown), implying that incorporation of Rpn10 protein lacking UIM domains into 26S proteasomes exerted a somewhat dominant-negative effect. However, these mice were fertile and showed no obvious phenotypes other than slow growth. $Rpn10^{\Delta UIM/+}$ mice were intercrossed to produce $Rpn10^{\Delta UIM/\Delta UIM}$ mice. The progeny did not contain any surviving $Rpn10^{\Delta UIM/\Delta UIM}$ pups, suggesting that the absence of the UIM domains of Rpn10 was incompatible with embryogenesis. Examination of embryos at various developmental stages revealed that the development of $Rpn10^{\Delta UIM/\Delta UIM}$ embryos was normal before E6.5 (data not shown) but appeared to be delayed at E8.5 (Fig. 3B and C). At E9.5, development arrested at a stage corresponding to E8.5 of the wild type; the turning process that results in a fetal position, normally seen at the transition from the 6-somite to the 8-somite stage, was not initiated (Fig. 3B and C). However, we could not find specific morphological defects in the embryos, such as disturbed formation of heart tubes, which are often associated with the failure of turning seen in other knockout mice such as GATA4 knockout mice (47). Intriguingly, $Rpn10^{\Delta UIM/\Delta UIM}$ embryos developed to an advanced stage compared to $Rpn10^{-/-}$ embryos, indicating that the VWA domain of Rpn10 rescued development from E6.5 to E9.5. These results suggest that the VWA domain alone plays some roles in proteasome function but that the UIM domain-dependent function of proteasomes is still required for mouse development, especially at the turning stage.

UIM domain deficiency in the liver is associated with impaired degradation of ubiquitinated proteins. To determine the biochemical basis of the significance of the UIM domain of Rpn10, we generated mice that expressed Rpn10ΔUIM exclusively in postnatal hepatocytes by crossing $Rpn10^{a/a}$ mice with transgenic mice that expressed Cre recombinase under the control of the albumin (Alb) promoter (28). $Rpn10^{a/a:Alb}$ mice, which expressed Rpn10ΔUIM proteins instead of Rpn10a proteins in the liver postnatally, were born without any abnormal appearance or developmental defect. We first confirmed the deletion of the UIM domains of Rpn10 in the liver. In the $Rpn10^{a/a:Alb}$ liver, no full-length Rpn10a proteins were detected. Instead, as expected, a truncated form of Rpn10 appeared, which could be detected by an anti-Rpn10 antibody raised against the VWA domain of Rpn10 [Rpn10(N)] but not by an anti-Rpn10 antibody raised against the UIM domain of Rpn10 [Rpn10(C)] (Fig. 4A). This Rpn10ΔUIM species was incorporated correctly into 26S proteasomes, consistent with the findings of studies with yeast (Fig. 4B). Interestingly, immunoblot analysis of liver lysates revealed that protein levels of subunits of the 20S proteasome (α6, α7), the base (Rpn1, Rpt3, Rpt5, Rpt6), and the lid (Rpn3, Rpn6, Rpn7), as well as levels of some proteasome-interacting proteins (mHR23B, USP14), were all increased in the $Rpn10^{a/a:Alb}$ liver (Fig. 4A). The up-regulation of proteasome subunits led to approximately twofold increases in the levels of 20S and 26S proteasomes and in proteasome-specific peptidase activities in $Rpn10^{a/a:Alb}$ liver lysates relative to those for $Rpn10^{a/a}$ liver lysates (Fig. 4C). To examine the reason for the increased proteasome levels, we quantified relative mRNA levels of proteasome subunits by real-time PCR analysis. We noted 1.8- to 2.5-fold increases in levels of mRNAs of proteasome subunits and proteasome-interacting proteins in the $Rpn10^{a/a:Alb}$ liver relative to those in the $Rpn10^{a/a}$ liver, indicating that transcription of overall proteasome-related genes was up-regulated in the $Rpn10^{a/a:Alb}$ liver (Fig. 4D). Despite the elevated amounts of proteasomes and the consequently increased peptidase activities, accumulation of polyubiquitin-conjugated proteins was noted in the $Rpn10^{a/a:Alb}$ liver (Fig. 4E). To test whether degradation of native proteins was impaired in the $Rpn10^{a/a:Alb}$ liver, we measured the degradation rates of two types of proteasome substrates in vitro. One is ODC, which is degraded by 26S proteasomes in a ubiquitin-independent but antizyme-dependent manner (26). The other is cIAP1 protein, a RING finger type ubiquitin ligase that ubiquitinates itself for degradation by 26S proteasomes in a ubiquitin-dependent manner (37). The degradation rate of ODC was increased in lysates of the $Rpn10^{a/a:Alb}$ liver, and this increase correlated with the increase in the level of the 26S proteasome (Fig. 4F, left). In contrast, the degradation rate of ubiquitinated cIAP proteins was markedly reduced in the $Rpn10^{a/a:Alb}$ liver, although the amounts of 26S proteasomes and mHR23B were larger than those in the $Rpn10^{a/a}$ liver (Fig. 4F, right). These results indicate that the UIM domain of Rpn10 plays an important role in the recognition and degradation of ubiquitinated proteins in the mouse liver. It is likely that increased transcription of proteasome-related genes is a feedback regulation mechanism to compensate for the impaired degradation and accumulation of ubiquitinated proteins, as was also observed for the Rpn10-deficient fly (40, 48).

Previous reports showed that human homologues of yeast Rad23 bind to proteasomes via the second UIM domain of human Rpn10 (7, 17, 25, 46), whereas Rad23 binds directly to Rpn1 in yeast (5, 32). To assess the significance of the UIM domains of Rpn10 in recruiting Rad23 species to proteasomes in mammals, we immunoprecipitated 26S proteasomes from liver lysates with an anti-Rpt6 antibody and compared the amount of proteasome-associated mHR23B (a mouse homologue of yeast Rad23) in Rpn10ΔUIM liver to that in $Rpn10^{a/a}$ liver by immunoblotting (Fig. 4G). Since Rpn10ΔUIM liver contained increased levels of proteasomes and proteasome activity (Fig. 4A and C), the amounts of proteasomes loaded were adjusted for the peptide-hydrolyzing activities of the ly-

Rpn10 gene. Exons 1 to 10 are shown as solid rectangles. The probe for Southern blot analysis is shown as a gray box. The positions of PCR primers are depicted as arrows. neo, neomycin-resistant cassette; DTA, diphtheria toxin gene. (C) Southern blot analysis of genomic DNAs extracted from mouse tails. Wild-type and knockout alleles were detected as 14-kb and 8-kb bands, respectively. (D) PCR analysis of genomic DNAs extracted from wild-type and $Rpn10^{+/-}$ mouse tails. (E) $Rpn10^{+/+}$ or $Rpn10^{+/-}$ (top) and $Rpn10^{-/-}$ (bottom) embryos at E6.5 and E7.5 were sagittally sectioned and stained with hematoxylin and eosin. (F) Impaired development of $Rpn10^{-/-}$ blastocysts in in vitro cultures. Genotypes were determined by PCR.